# SANDIA REPORT

SAND2009-5544
Unlimited Release
Printed August 2009

# Survey of Four Damage Models for Concrete

Rebecca M. Brannon and Seubpong Leelavanichkul

Prepared by
Sandia National Laboratories
Albuquerque, New Mexico 87185 and Livermore, California 94550

Sandia is a multiprogram laboratory operated by Sandia Corporation,
a Lockheed Martin Company, for the United States Department of Energy's
National Nuclear Security Administration under Contract DE-AC04-94-AL85000.



Issued by Sandia National Laboratories, operated for the United States Department of Energy by Sandia Corporation.



Available to DOE and DOE contractors from
U.S. Department of Energy
Office of Scientific and Technical Information
P.O. Box 62
Oak Ridge, TN 37831

Telephone: (865) 576-8401
Facsimile: (865) 576-5728
E-Mail: reports@adonis.osti.gov
Online ordering: http://www.osti.gov/bridge

Available to the public from
U.S. Department of Commerce
National Technical Information Service
5285 Port Royal Rd
Springfield, VA 22161

Telephone: (800) 553-6847
Facsimile: (703) 605-6900
E-Mail: orders@ntis.fedworld.gov
Online ordering: http://www.ntis.gov/help/ordermethods.asp?loc=7-4-0#online

SAND2009-5544
Unlimited Release
Printed August 2009

# Survey of Four Damage Models for Concrete

Rebecca M. Brannon and Seubpong Leelavanichkul
Department of Mechanical Engineering
University of Utah
50 S. Campus Dr.
Salt Lake City, UT 84109
brannon@mech.utah.edu
sleelava@eng.utah.edu

Sandia Contract No. 903761

**Abstract**

Four conventional damage plasticity models for concrete, the Karagozian and Case model (K&C), the Riedel-Hiermaier-Thoma model (RHT), the Brannon-Fossum model (BF1), and the Continuous Surface Cap Model (CSCM) are compared. The K&C and RHT models have been used in commercial finite element programs many years, whereas the BF1 and CSCM models are relatively new. All four models are essentially isotropic plasticity models for which "plasticity" is regarded as any form of inelasticity. All of the models support nonlinear elasticity, but with different formulations. All four models employ three shear strength surfaces. The "yield surface" bounds an evolving set of elastically obtainable stress states. The "limit surface" bounds stress states that can be reached by any means (elastic or plastic). To model softening, it is recognized that some stress states might be reached once, but, because of irreversible damage, might not be achievable again. In other words, softening is the process of collapse of the limit surface, ultimately down to a final "residual surface" for fully failed material. The four models being compared differ in their softening evolution equations, as well as in their equations used to degrade the elastic stiffness. For all four models, the strength surfaces are cast in stress space. For all four models, it is recognized that scale effects are important for softening, but the models differ significantly in their approaches. The K&C documentation, for example, mentions that a particular material parameter

affecting the damage evolution rate must be set by the user according to the mesh size to preserve energy to failure. Similarly, the BF1 model presumes that all material parameters are set to values appropriate to the scale of the element, and automated assignment of scale-appropriate values is available only through an enhanced implementation of BF1 (called BFS) that regards scale effects to be coupled to statistical variability of material properties. The RHT model appears to similarly support optional uncertainty and automated settings for scale-dependent material parameters. The K&C, RHT, and CSCM models support rate dependence by allowing the strength to be a function of strain rate, whereas the BF1 model uses Duvaut-Lion viscoplasticity theory to give a smoother prediction of transient effects. During softening, all four models require a certain amount of strain to develop before allowing significant damage accumulation. For the K&C, RHT, and CSCM models, the strain-to-failure is tied to fracture energy release, whereas a similar effect is achieved indirectly in the BF1 model by a time-based criterion that is tied to crack propagation speed.

# Contents

# List of Figures

# List of Tables

# Nomenclature

| | |
|---|---|
| $f_t$ | tensile strength |
| $f'_c$ | compressive strength |
| $\sigma^T$ | trial elastic stress |
| $\mathbf{S}$ | stress deviator |
| $\sigma_1, \sigma_2, \sigma_3$ | principal stresses |
| $I_1, J_2, J_3$ | invariants |
| $\sigma_A$ | axial stress |
| $\sigma_L$ | lateral stress |
| $f$ | yield function |
| $F_f$ | strength surface |
| $\Gamma(\theta, I_1)$ | lode angle function |
| $\psi$ | ratio of the tensile to compressive meridian radii at a given pressure |
| $Y_m, Y_r, Y_y$ | limit, residual, and yield surface |
| $a_k$ | parameters defining strength surfaces |
| $\lambda$ | Effective plastic strain parameter |
| $\varepsilon_{ij}, \delta\varepsilon_{ij}$ | strain tensor and strain increments |
| $\dot{\varepsilon}, \delta\dot{\varepsilon}$ | effective strain rate and effective strain rate increments |
| $\varepsilon_v, \varepsilon_v^p$ | volumetric strain and plastic volumetric strain |
| $\sigma, \sigma^{vp}, \sigma^d$ | stress tensor (general, viscoplastic, damage) |
| $r_f$ | rate enhancement factor |
| $DIF$ | dynamic increasing factor |
| $\eta$ (K&C) | damage |
| $\phi$ | potential function |
| $\mu$ | scalar factor governing the magnitude of the plastic flow |
| $\mathbf{C}$ | stiffness tensor |

| | |
|---|---|
| $G$ | shear modulus |
| $K, K_U, K_L$ | bulk modulus, unloading bulk modulus, loading bulk modulus |
| $\varphi$ | scale factor for bulk modulus used in K&C model |
| $\nu$ | Poisson's ratio |
| $\alpha, \beta$ | rate effects exponents used in RHT model |
| $p_{\text{spall}}$ | concrete spall strength used in RHT model surface |
| $F_c$ | elliptical cap function |
| $X$ | cap location |
| $\kappa$ | cap initiation |
| $BQ$ | brittle to ductile transition factor |
| $D_1, D_2$ (RHT) | damage parameters |
| $w_u$ | element characteristic length (crack width) |
| $l$ | characteristic crack length |
| $G_F$ | Fracture energy |
| $b_k, g_k$ (BF1) | nonlinear bulk and shear moduli parameters |
| $\xi, \alpha$ | shifted stress tensor and backstress |
| $h_k, C_H$ | hardening modulus |
| $\mathbf{H}_k$ | hardening tensor |
| $N$ (BF1) | isotropic hardening shift factor |
| $G(\alpha)$ | decay function |
| $\tau$ | characteristic time |
| $\sigma^L, \sigma^H$ | Low and high rate stresses |
| $\eta$ | viscoplastic interpolation |
| $N_H$ (CSCM) | hardening initiation |
| $\tau_b$ | brittle damage threshold |
| $\tau_s$ | ductile damage threshold |
| $r_{ob}, r_{od}, r_o$ | initial damage threshold (brittle, ductile, general) |
| $\gamma$ (CSCM) | rate effect fluidity parameter |
| $\alpha_s, \beta_s . \delta_s, \gamma_s$ | $DIF$ parameters |

# Chapter 1

# Introduction

A persistent challenge in simulating damage of concrete structures is the development of efficient and accurate constitutive models. The desired models need to produce a smooth transition from a linear or nonlinear elastic range to a non-linear hardening regime and ultimately a weak post-peak state. This report compares four concrete material models: (1) the Karagozian and Case model (K&C), (2) the Riedel-Hiermaier-Thoma model (RHT), (3) the Brannon-Fossum model (BF1), and (4) the Continuous Surface Cap Model (CSCM). To facilitate discussion of these models, a common terminology will be adopted for concepts common to all four models. The performance of each model is assessed by making comparison between some simulations.

Unconfined concrete tensile strength ($f_t$) can be as much as 92% lower than the compressive strength ($f'_c$) [11]. The ultimate strength of concrete depends on the pressure and shear stresses. At low pressure, the inelastic behavior of concrete material is not related to the motion of dislocations as for metallic materials. In uniaxial loading, deformation is approximately linear in the elastic regime. As the deformation increases, the cracks increase in size and number, and then eventually propagate through the material to culminate in ultimate failure.

In extension, the active crack planes are orthogonal to the load direction. In compression, they are parallel to the load direction (i.e., misaligned cracks will kink in this direction). In either case, crack planes tend to form orthogonal to the direction of the least compressive (or most tensile) principal stress. A peak stress is reached at a point where microcracking has caused sufficient degradation of stiffness such that the material would become unstable if loaded in stress control. If hydrostatic pressure is present, a fully damaged material in compression retains a residual strength such as that of a granular medium.

A distinctive behavior of concrete and other quasibrittle materials is the phenomenon of dilatation (i.e., volume increase) under inelastic compressive loading. Although compressive stresses initially induce a volume reduction, continued compression induces material damage in the form of shear cracking. Subsequent dilatation is typically attributed to geometrically necessary introduction of void space associated with crack kinking. Standard concrete exhibits volume expansion under compressive loading at low confining pressure, but does not dilatate at high confining pressure greater than 100MPa [11].

For triaxial tests conducted under sufficiently high confining pressure, crack growth tends to be negligible in comparison to porosity changes. For purely hydrostatic loading, a porous equation of state is usually employed to model three different phases: elastic deformation, compaction, and

solidification. During the compaction phase, pores in the material collapse. In the final solidification phase, the material is approximately homogeneous (because pore space has been fully crushed out), and the volumetric response is once again elastic.

All four models in this report fall loosely in the category of generalized isotropic plasticity theory. Specifically, they all presume existence of an elastic domain. The boundary of this domain in stress space is called the "yield surface" even though mechanisms of inelasticity are not necessarily associated with dislocations. Because all four models are isotropic, the yield surface in stress space has a certain degree of symmetry about the hydrostat. The radial distance from the hydrostat is a measure of equivalent shear stress. The detail of the surfaces used in these models is discussed in upcoming chapters.

# General formulation

The implementation of the concrete models under investigation can be broken into (1) elastic and plastic updates, (2) strength surface formulations, (3) rate and scale effects, and (4) damage accumulation. The models differ in their approaches to these areas. This report does not cover the details of elastic and plastic updates used in each model because all of them follow the typical elasticity and plasticity theories. All of the models under investigation currently presume that the concrete is initially isotropic. The BF1 and CSCM models support developed anisotropy in the rudimentary form of kinematic hardening. Neither the K&C nor RHT models support intrinsic (i.e. pre-existing) elastic anisotropy, but the BF1 model includes support for joints in the concrete and the CSCM model includes support for rebar. All models support nonlinear elasticity, implemented in incremental form such that stress increments are linear and isotropic in strain increments with the tangent bulk and shear moduli varying with deformation or stress.

Depending on the type of loads, the concrete will eventually yield or fail. The yield threshold is defined by the yield surface that is described in the following chapter. During compaction, the material is tentatively presumed to be elastic thus giving a trial elastic stress $\sigma^T$. If $\sigma^T$ is found to lie outside the yield surface, the tentative assumption is rejected, and the loading increment is re-evaluated using plastic update equations. When damage occurs and begins to accumulate, the strength of the concrete is reduced by appropriately collapsing the strength surface in stress space.

High loading rates are well known to lead to an apparent increase in strength. In the K&C and RHT models, this behavior is accommodated by expanding the yield surface so that higher stress levels are required to reach it. The BF1 and CSCM models account for rate dependence through a viscoplastic approach that better matches stress transients prior to reaching the steady state strength.

# Shear strength surface

To include the effects of material strength and resistance to shear distortion, one can work with the stress deviator $\mathbf{S}$, which is defined as the difference between the total stress, $\sigma$, and a uniform hydrostatic pressure, $p$,

$$\mathbf{S} = \sigma - p\mathbf{I} \qquad \text{or} \qquad \mathbf{S} = \sigma - \frac{1}{3}\text{tr}(\sigma)\mathbf{I}. \tag{1.1}$$

where the hydrostatic pressure (or mean stress) can be represented by one third of the first invariant, $I_1$, of the total stress.

$$p = \frac{1}{3}(\sigma_1 + \sigma_2 + \sigma_3) = \frac{1}{3}\text{tr}\sigma = \frac{I_1}{3}.$$

The second and the third invariants are given by

$$J_2 = \frac{1}{2}\text{tr}(\mathbf{S}^2), \qquad \text{and} \qquad J_3 = \frac{1}{3}\text{tr}(\mathbf{S}^3). \tag{1.2}$$

All four concrete models investigated in this report rely heavily on axisymmetric compressive stress data. The mechanics invariants for axisymmetric loading having an axial stress $\sigma_A$ and two equal lateral stresses $\sigma_L$ are

$$I_1 = \sigma_A + 2\sigma_L, \quad J_2 = \frac{1}{3}(\sigma_A - \sigma_L)^2, \qquad J_3 = \frac{2}{27}(\sigma_A - \sigma_L)^3. \tag{1.3}$$

For elastic distortion, after loading and unloading, all the distortion energy is recovered and the material returns to its initial configuration. However, when the distortion is large enough that the material reaches its elastic limit, only elastic distortion energy is recovered. The material suffers permanent plastic strain and can therefore no longer return to its initial configuration. Hence, a yield function is used to describe the material elastic limit and the subsequent transition to plastic flow.

The yield criterion for all four concrete models in this report can be written in the form

$$\sqrt{J_2} = F_f(I_1, \theta, \kappa), \tag{1.4}$$

where $\sqrt{J_2}$, $I_1$, and $\theta$ are stress invariants, and $\kappa$ stands for one or more internal variables. The stress invariant $I_1$ is proportional to pressure (specifically, $I_1 = 3p$) and also proportional to the axial coordinate of the stress state along the hydrostat in principal stress space. The stress invariant

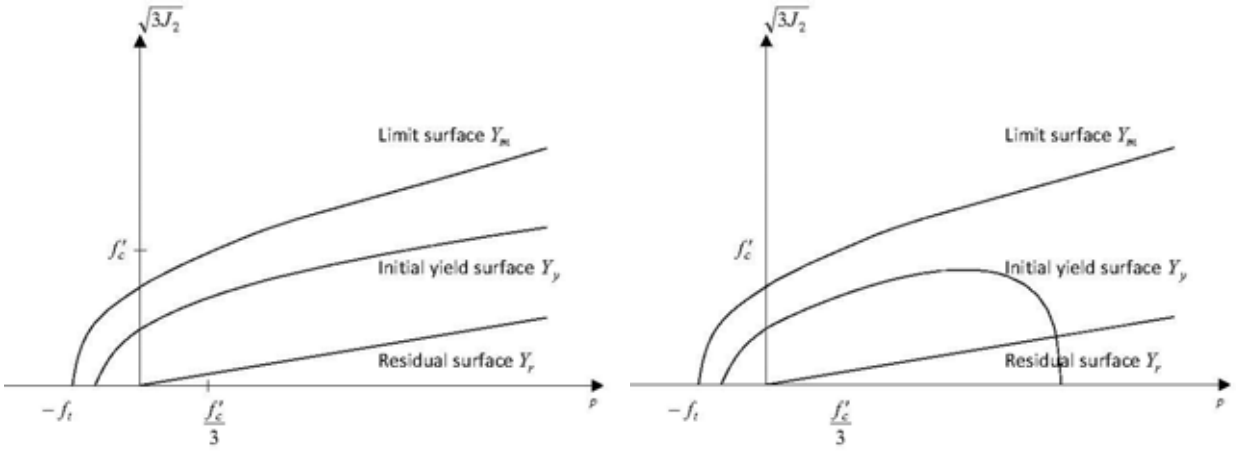


**Figure 1.1.** Left: yield surface without cap. Right: yield surface with cap.

$\sqrt{J_2}$ is proportional to equivalent shear stress and also proportional to the radial distance of the stress state from the hydrostat in stress space. The Lode angle stress invariant $\theta$ serves as an alternative to the third invariant, $J_3$, and it quantifies the angular coordinate of the stress state in principal stress space.

The above yield criterion corresponds to the following yield function

$$f = J_2 - [F_f(I_1, \theta, \kappa)]^2 = 0, \tag{1.5}$$

Equation (1.4) and (1.5) are the basic forms employed by the K&C and RHT models. The BF1 and CSCM models include extra terms that account for backstress, but can also be reduced to the same expression as the other two models. The full expressions of the yield function used in the BF1 and CSCM models are given later in Chapters 4 and 5, respectively. In addition to the yield surface, all four concrete models use two additional surfaces to describe the peak stress limit of the material. The "limit surface" bounds the set of stress states that are achievable at least once. After a stress state at the limit surface has been reached, irreversible damage occurs in the material causing the boundary of achievable stress states to shrink until ultimately reaching a residual surface corresponding to a "fully damaged" state. These three strength surfaces are sketched in Fig. 1.1. The limit and residual surfaces are stationary, while the current yield surface evolves in response to evolution of internal variables that directly or indirectly account for porosity and microcracks. The equations representing these surfaces are given in more detail in Chapters 2, 3, and 4.

Figure 1.1(right) shows the capped yield surface shape that is typical of models that account for porosity. Not only does the cap introduce an elastic limit in pure hydrostatic compression, it also allows porosity to affect the shear strength. This approach is adopted in the RHT, BF1, and

CSCM models. However, the K&C model allows for a hydrostatic elastic limit only through an equation of state, which does not include the effect of porosity on shear strength.

# Octahedral profile

Cylindrical Lode coordinates $(r,\theta,z)$ represent an alternative invariant triplet that can be obtained from the conventional invariant triplet ($I_1$, $J_2$, and $J_3$) as follows [12]:

$$r=\sqrt{2J_2} \qquad , \qquad \sin 3\theta = \frac{J_3}{2}\left(\frac{3}{J_2}\right)^{3/2} \qquad , \qquad z=\frac{I_1}{\sqrt{3}}. \tag{1.6}$$

With this definition of the Lode angle, triaxial compression corresponds to a Lode angle of 30°. The Lode angle dependence in Eqs. (1.4) and (1.5) is accomplished by multiplying the compressive meridian, $F_f(I_1,30^\circ,\kappa)$ in Fig. 1.1, by a scale function $\Gamma(\theta,I_1)$. This Lode angle scale function is a ratio of the radius of the octahedral cross section at an angle $\theta$ to the radius of the compressive meridional profile at angle 30°. Various formulations for the scale function have been used in the literature. Of these, the following are common choices:

1. Willam-Warnke function [38]:

$$\Gamma(\theta) = \frac{4\left(1-\psi^2\right)\cos^2\alpha^* + (1-2\psi)^2}{2\left(1-\psi^2\right)\cos\alpha^* + (2\psi-1)\sqrt{4\left(1-\psi^2\right)\cos^2\alpha^* + 5\psi^2 - 4\psi}}, \tag{1.7}$$
$$\text{where } \alpha^* = \pi/6+\theta, (0.5 \le \psi \le 2),$$

2. Mohr-Coulomb [33]:

$$\Gamma(\theta) = \frac{2\sqrt{3}}{3-3\left(\frac{1-\psi}{1+\psi}\right)}\left(\cos\theta - \frac{3\left(\frac{1-\psi}{1+\psi}\right)\sin\theta}{\sqrt{3}}\right) \qquad (0.5 \le \psi \le 2), \tag{1.8}$$

3. Gudehus [15]:

$$\Gamma(\theta) = \frac{1}{2}\left[1+\sin 3\theta + \frac{1}{\psi}\left(1-\sin 3\theta\right)\right] \qquad (7/9 \le \psi \le 9/7). \tag{1.9}$$

Here, $\psi$ is the ratio of the radius, $r_t$, at the tensile meridian (where $\theta=-30^\circ$) to the radius, $r_c$, of the compressive meridian. The octahedral cross-sections corresponding to these Lode angle scale functions are illustrated in Fig. 1.2 for various values of the strength ratio parameter $\psi$. Note that the functions are normalized to coincide at the compressive meridian. All four models investigated in this report support Willam-Warnke Lode angle function. The BF1 model also allows the options of Mohr-Coulomb and Gudehus.

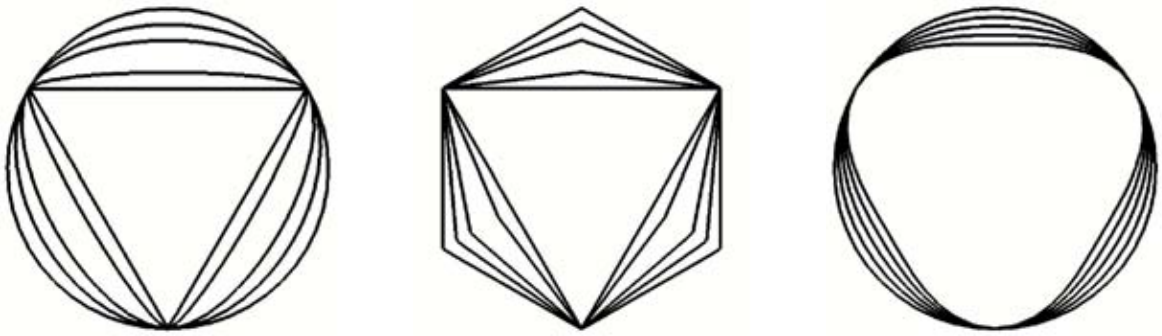

**Figure 1.2.** Deviatoric section: (*left*) Willam-Warnke, (*center*) Mohr-Coulomb, and (*right*) Gudehus.

# Chapter 2

# The K&C Concrete Model

## Strength surfaces

The K&C model uses stress differences to describe the yield surface ($\Delta\sigma_y$), the limit surface ($\Delta\sigma_m$), and the residual surface ($\Delta\sigma_r$). In view of Eq.(1.3), where the stress difference is $(\sigma_A - \sigma_L)$, the stress difference can be written as $\sqrt{3J_2}$, which allows generalization of the theory to general stress states. During the initial loading or reloading, the stresses are elastic until an initial yield surface is reached. The initial yield surface hardens to the limit surface or softens to the residual surface, depending on the nature of loading or on the material state. Three fixed surfaces are used in the K&C model and are defined as

$$Y_y = \Delta\sigma_y = a_{0y} + \frac{p}{a_{1y} + a_{2y}p} \qquad \text{(yield surface)}, \tag{2.1}$$

$$Y_m = \Delta\sigma_m = a_{0m} + \frac{p}{a_{1m} + a_{2m}p} \qquad \text{(limit surface)}, \tag{2.2}$$

$$Y_r = \Delta\sigma_r = a_{0f} + \frac{p}{a_{1f} + a_{2f}p} \qquad \text{(residual surface)}, \tag{2.3}$$

where the $a$-parameters are user inputs, and $a_{0f} = 0$ for concrete. The three surfaces are defined by different values of the $a$-parameters. To facilitate comparing the K&C model to other models, Eqs. (2.1) to (2.2) can be recast in terms of standard invariants as follows:

$$\sqrt{J_2} = F(I_1), \tag{2.4}$$

where

$$F(I_1) = \frac{1}{\sqrt{3}}\left(a_{0m} + \frac{I_1}{3a_{1m} + a_{2m}I_1}\right)$$

The K&C concrete model uses Willam-Warnke's Lode-angle function $\Gamma(\theta)$ shown in Eq. (1.7) to describe the octahedral cross section of the surfaces. If tensile data are available instead of

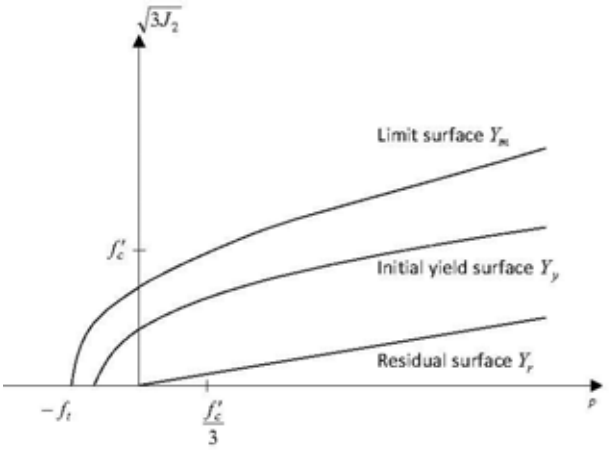


**Figure 2.1.** K&C meridian profiles

compressive data, the compressive meridian can be approximated by dividing the tensile meridian $\Delta\sigma$ by the relative distance between the compression and tension meridian $\psi(p)$ at each pressure $p$. The above equations apply only for compressive pressures. For tensile pressure, these equations are replaced by

$$\Delta\sigma = \frac{3}{2}(p + f_t) \qquad \text{or} \qquad F(I_1) = \frac{\sqrt{3}}{2}\left(\frac{I_1}{3} + f_t\right). \tag{2.5}$$

Equation (2.5) ensures conditions given in [8, 25] are met (i.e., $\Delta\sigma$ passes through $(p, \Delta\sigma) = (-f_t, 0)$ under triaxial test and $(p, \Delta\sigma) = (-f_t/3, f_t)$ for uniaxial test). Illustrated below is a complete linear piecewise definition of $\psi(p)$ as given in [28] for this model:

$$\psi(p) = \begin{cases} \frac{1}{2} & : \quad p \le 0, \\ \frac{1}{2} + \frac{3}{2}\left(\frac{f_t}{f_c'}\right) & : \quad p = f_c'/3, \\ \frac{\alpha f_c'}{a_0 + \frac{2\alpha f_c'/3}{a_1 + 2a_a \alpha f_c'/3}} & : \quad p = 2\alpha f_c'/3, \\ 0.753 & : \quad p = 3f_c', \\ 1 & : \quad p \ge 8.45 f_c', \end{cases} \tag{2.6}$$

where $\alpha$ is a scalar factor multiplying $f_c'$ to denote the location where the failure occurs. The function given in Eq. (2.6) is linear between the specified points. For example, Kupfer *et al.*[25] showed in biaxial compression tests that the failure occurred at $(\sigma_1, \sigma_2, \sigma_3) = (0, \alpha f_c', \alpha f_c')$, with $\alpha \approx 1.15$. Even though the K&C model allows $\psi$ to be pressure-dependent, a slope discontinuity is present due to the piecewise representation of $\psi$.

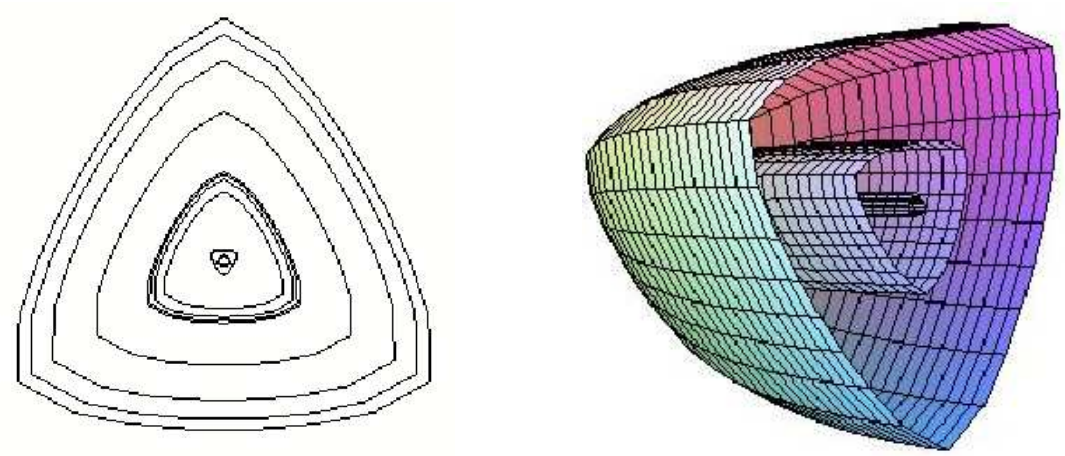

**Figure 2.2.** Failure surfaces in 3D stress space

# Rate and scale dependence

The K&C model uses rate effects to handle shear damage accumulation. A strain rate enhancement factor $r_f$ is used to scale the strength surface when the material is subjected to a high loading rate. This strength enhancement factor is called the dynamic increasing factor ($DIF$) in the CEB-FIP model code 90 (Comité Euro-International du Béton and Fédération International de la Précontrainte) [35], see Fig. 2.3

When pressure $p$ is returned from the equation of state, an "unenhanced" pressure $p/r_f$ and "unenhanced" (i.e., quasistatic) shear strength $F(I_1/r_f)$ are computed. Multiplying the strain rate enhancement factor $r_f$ (or $DIF$) to $F(I_1/r_f)$, a new enhanced limit surface at the current pressure $p$ is obtained:

$$\Delta\sigma_e = r_f \Delta\sigma\left(\frac{p}{r_f}\right) \qquad \text{or} \qquad F_e(I_1) = r_f F\left(\frac{I_1}{r_f}\right). \tag{2.7}$$

To include the strain rate enhancement factor $r_f$ (or $DIF$), a modified effective plastic strain is defined as

$$\lambda = h\sqrt{\frac{2}{3}\varepsilon_{ij}^p \varepsilon_{ij}^p}, \tag{2.8}$$

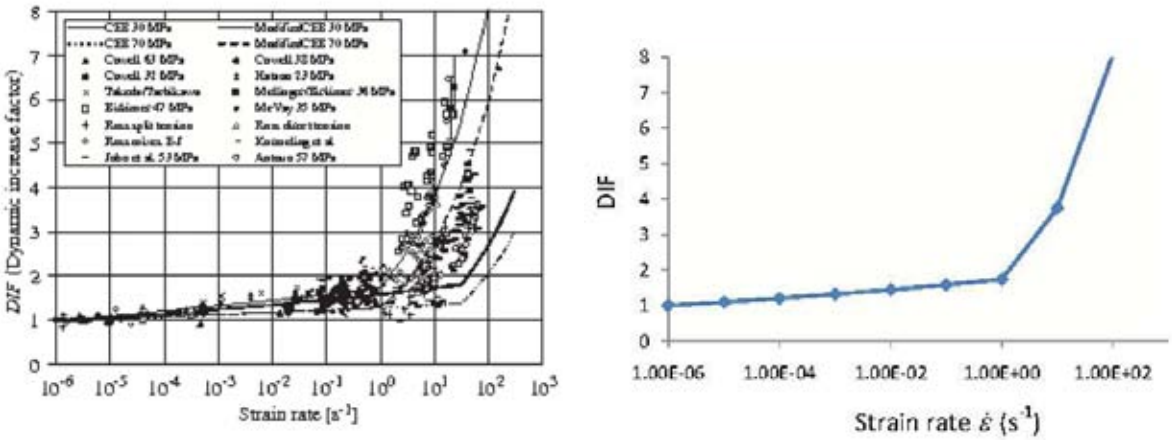


**Figure 2.3.** Experimental data for *DIF* according to CEB-FIB design model code [26].

where

$$h = \begin{cases} \dfrac{1}{r_f\left(1+\frac{p}{r_f f_t}\right)^{b_1}} & \text{for } p \geq 0 \qquad \text{(compression)}, \\ \dfrac{1}{r_f\left(1+\frac{p}{r_f f_t}\right)^{b_2}} & \text{for } p < 0 \qquad \text{(tension)}. \end{cases} \tag{2.9}$$

Equation (2.9) allows the damage accumulation to be different in tension and compression. The $b_1$ and $b_2$ parameters are fitted to experimental data. The input scalar parameter $b_2$ governs the softening part of the unconfined uniaxial tension stress-strain curve as the stress point moves from the limit to the residual surface, while $b_1$ governs the softening for compression.

Damage due to isotropic tensile stressing is handled by adding a volumetric damage accumulation that is computed by incrementing the effective plastic strain parameter by $\Delta\lambda$ according to

$$\triangle\lambda = b_3 f_d k_d(\varepsilon_v - \varepsilon_{v,\text{yield}}), \tag{2.10}$$

where $b_3$ is an input parameter, $\varepsilon_v$ is volumetric strain, $\varepsilon_{v,\text{yield}}$ is the volumetric strain at yield. The factor $f_d$ limits the effect of this change according to proximity of the stress state to the hydrostat. Specifically,

$$f_d = \begin{cases} 1 - \frac{|\sqrt{3J_2}/p|}{0.1} & : \quad 0 \leq |\sqrt{3J_2}/p| < 0.1, \\ 0 & : \quad |\sqrt{3J_2}/p| \geq 0.1. \end{cases} \tag{2.11}$$

Determination of the input parameters $b_1, b_2$, and $b_3$ is described in [28]. The parameter $b_2$ is computed iteratively using the data from the unconfined uniaxial tensile test until the area under

the stress-strain curve coincides with $G_F/w_u$ where $G_F$ is the fracture energy, and $w_u$ is crack front width (which equals the element size). Therefore, different values of $b_2$ must be used for different element sizes; otherwise the computed energy release will be incorrect. Whether or not this adjustment of $b_2$ is automated is unclear.

# Damage accumulation

Once the initial yield surface is reached, the stress state is evolved by interpolating between Eq. (2.1) and Eq. (2.2) according to

$$\Delta\sigma = \eta\,(\Delta\sigma_m - \Delta\sigma_y) + \Delta\sigma_y \qquad \text{or} \qquad F(I_1) = \eta\,[F_m(I_1) - F_y(I_1)] + F_y(I_1), \tag{2.12}$$

where a user defined damage function $\eta$ indicates the location of the current yield surface relative to limit surface and is a function of an effective plastic strain parameter,

$$\lambda = \int_0^t \sqrt{\frac{2}{3}\dot{\varepsilon}^p : \dot{\varepsilon}^p}\,dt \tag{2.13}$$

The damage $\eta$ is initially zero at $\lambda = 0$ and increases to unity at a user-specified value $\lambda_m$ marking the onset of softening. During softening, $\eta$, which now decreases as $\lambda$ increases, is used to interpolate the current surface between limit and residual surfaces, Eq. (2.2) and Eq. (2.3), respectively according to

$$\Delta\sigma = \eta\,(\Delta\sigma_m - \Delta\sigma_r) + \Delta\sigma_r \qquad \text{or} \qquad F(I_1) = \eta\,[F_m(I_1) - F_r(I_1)] + F_r(I_1), \tag{2.14}$$

Typical $\eta(\lambda)$ used in the K&C model has behavior as illustrated in Fig. 2.4.

The experimental data presented in [8, 25] showed that the principal stress difference should be approximately $f_t$ for biaxial compression and triaxial tension tests. To be able to reach this point, the K&C model initially sets a value of pressure cutoff $p_c$ to $-f_t$. This choice is consistent with a maximum principal stress criterion at tensile pressures. If stresses reach the failure threshold in the negative pressure range, the parameter $\eta$ is then used to move the pressure cutoff from $-f_t$ to zero in a smooth fashion. This is done by checking the pressure returned by the equation of state (EOS), and resetting it to $p_c$ using the following conditions

$$p_c = \begin{cases} -f_t & \text{if the limit surface has not been reached (hardening),} \\ -\eta f_t & \text{if the limit surface has been reached (softening).} \end{cases}$$

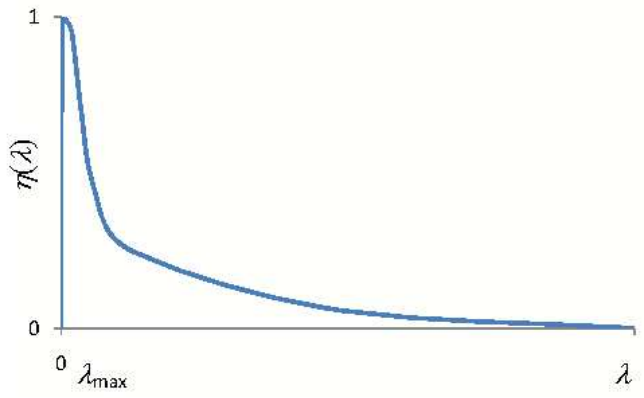


**Figure 2.4.** Example of damage function $\eta(\lambda)$.

# Plastic update

The cut-off pressure is reduced during the process of softening, and can cause a segment of the meridian in the negative pressure portion to become very steep. To avoid a steep slope in this region, the limit surface $\eta Y(p,\eta)$ in Eq. (2.2) is modified according to

$$\eta Y_1(p,\eta) \quad = \quad \eta\left(\Delta\sigma_m(p) - \frac{p_f - p}{p_f - p_c(\eta)}\Delta\sigma_m(p_c)\right) = 3\,(p+\eta f_t)\,, \tag{2.15}$$

where $\Delta\sigma_m = 3(p+f_t)$ is the nominal limit surface in compression,
$p_f = 0$ is the intersection of the residual surface with the pressure axis, and
$p_c = -\eta f_t$ is the intersection of the limit surface with the pressure axis.

Hence, the current modified limit surface during the softening can be written as

$$Y(p,\eta) = \begin{cases} \eta\Delta\sigma_m(p) + (1-\eta)\Delta\sigma_f(p) & \text{for} \quad p > 0, \\ 3\,(p+\eta f_t) & \text{for} \quad p \le 0, \end{cases} \tag{2.16}$$

where $\Delta\sigma_f$ is the current unmodified failure surface. When the radial rate enhancement is used, the surface is computed as a function of $p/r_f$ and then multiplied by $r_f$ as shown in Eq. (2.7).

At any time step, the shear strength changes with both pressure $p$ and damage $\eta$. The current strength $Y$ is initially updated only according to the current pressure. The fully updated surface is then determined iteratively accounting for the updated damage $\eta$. Let $Y^*$ be the strength corresponding to the updated pressure but before the value of $\eta$ is determined. Then the fully updated strength $Y_{n+1}$ is determined as a result of the change in $\eta$ according to

$$Y_{n+1} - Y^* = \frac{\partial Y}{\partial \eta} d\eta = \frac{\partial Y}{\partial \eta}\frac{d\eta}{d\lambda} d\lambda \tag{2.17}$$

Using Eq. (2.8),

$$Y_{n+1} - Y^* = \frac{\partial Y}{\partial \eta}\frac{d\eta}{d\lambda}h(\sigma)\sqrt{\frac{2}{3}d\varepsilon_{ij}^p : d\varepsilon_{ij}^p}. \tag{2.18}$$

As is typical in plasticity models, the strain increment is decomposed into elastic and plastic parts ($d\varepsilon = d\varepsilon^e + d\varepsilon^p$). A conventional regular associated flow rule is adopted, and the stress state is updated in a conventional manner (see, e.g., [1]).

# Shear and bulk moduli

Prior to yielding, Hooke's law is used for the elastic stress-strain relationship. The K&C model supports nonlinear elasticity by permitting the moduli to vary with pressure. The shear modulus is computed from a user specified Poisson's ratio and the bulk modulus. It was commented in [28] that when the difference between the loading and unload/reload bulk moduli is large, a negative effective Poisson's ratio may occur. Therefore, the bulk modulus is entered as part of the EOS input set and is scaled within the the K&C model using a factor $\varphi$ depending on how far the pressure is below the "virgin curve" [28] (loading portion of the user's specified pressure vs. volumetric curve).

$$\varphi = \frac{-\Delta\varepsilon}{-\Delta\varepsilon + (p - p_f)/K_U}, \tag{2.19}$$

where $\Delta\varepsilon = \varepsilon_{v,\min} - \varepsilon_v$,
$\varepsilon_v$ is volumetric strain, and
$K_U$ is the unload/reload bulk modulus from the EOS.

The shear modulus is then calculated from the scaled bulk modulus $K'$ as

$$G = \frac{(1.5 - 3\nu)K'}{1+\nu}, \tag{2.20}$$

where $K' = (K_L - K_U)e^{-5.55\varphi} + K_U$, and $K_L$ is the loading modulus.

The constant 5.55 is chosen such that the $K'$ increases half way to unload/reload value when $p$ dropped $1/8$ of the way from the virgin curve to $p = p_f$ ($p_f = 0$ for concrete). According to Eq. (2.20), a user is required to input only a Poisson's ratio for the K&C model to compute the shear modulus.

# Chapter 3

# The RHT Concrete Model

This chapter discusses a material model for concrete using the RHT concrete model that has the following capability associated with brittle material

- Pressure hardening,
- Strain hardening,
- Strain rate hardening,
- Third invariant dependence for compressive and tensile meridians,
- Damage effects (strain softening), and
- Crack-Softening.

The above terminology was taken directly from ANSYS AUTODYN product features [6]. It is unclear what is meant by pressure hardening, but we suspect that it merely refers to increased shear strength with pressure. If so, the term hardening is used here in a nonstandard way.

## Strength surfaces

Similar to the K&C model, three strength surfaces are used in the RHT material model (see Fig. 3.1). The RHT concrete model expresses these surfaces in terms of the compressive meridian $Y_{TXC}(p)$, a rate factor $r_f = r_f(\dot{\varepsilon})$ (denoted as $F_{rate}(\dot{\varepsilon})$ in [18]), and the ratio of compressive and tensile radii $\Gamma(\theta)$. Willam-Warnke's Lode-angle function $\Gamma(\theta)$ is used in this model.

The strength along the compressive meridian is expressed as a triaxial compression normalized to the unconfined compression strength $f'_c$

$$Y^*_{TXC} = \frac{Y_{TXC}}{f'_c} = a_1 \left[ \frac{p}{f'_c} - \frac{p_{spall}}{f'_c} r_f \right]^{a_2} \quad \text{or} \quad F(I_1) = \frac{a_1}{\sqrt{3}} \left[ \frac{I_1}{3} - r_f p_{spall} \right]^{a_2}, \tag{3.1}$$

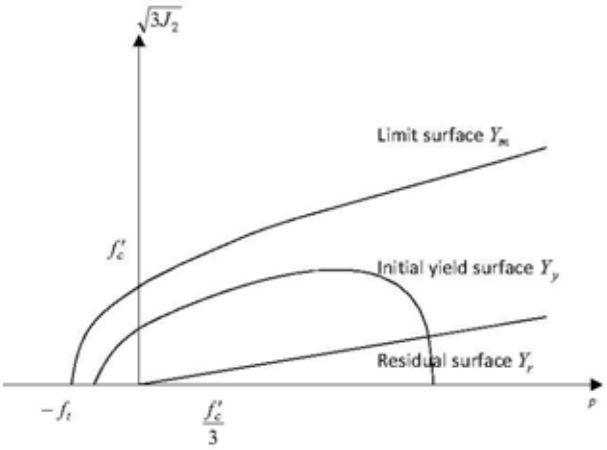


**Figure 3.1.** Failure surfaces

where

$$
\begin{aligned}
r_f &= \begin{cases} \left(\frac{\dot{\varepsilon}}{\dot{\varepsilon}_0}\right)^{\alpha} & : \quad p > f'_c, \text{ with } \dot{\varepsilon}_0 = 30 \times 10^{-6}\ \mathrm{s}^{-1}, \\ \left(\frac{\dot{\varepsilon}}{\dot{\varepsilon}_0}\right)^{\beta} & : \quad p < f'_c, \text{ with } \dot{\varepsilon}_0 = 3 \times 10^{-6}\ \mathrm{s}^{-1}, \end{cases} \\
a_1 &= \text{Initial slope of failure surface,} \\
a_2 &= \text{Pressure dependence of failure surface,} \\
P_{spall} &= \text{Spall strength,} \\
p &= \text{Pressure,} \\
\alpha &= \text{Material constant,} \\
\beta &= \text{Material constant.}
\end{aligned}
$$

Unlike the K&C model, which apparently does not model porosity effects on strength, the RHT model provides an option of an elliptical cap function $F_c(p)$ that closes the yield surface at high pressure, see Fig. 3.2.

$$
F_c(p) = \begin{cases} 1 & : \quad p \le \kappa, \\ \sqrt{1 - \left(\frac{p-\kappa}{X-\kappa}\right)} & : \quad \kappa < p < X, \\ 0 & : \quad p \ge X. \end{cases} \tag{3.2}
$$

where $\kappa$ is a pressure at which the uniaxial compression path intercepts with the elastic surface, and $X$ is the pressure where the yield surface intersects with the hydrostat axis. In the RHT model, $X = f'_c/3$, which is close to the pore crush pressure. This feature is not available in the K&C material model. The yield surface in the RHT model is determined through three parameters: the ratio of

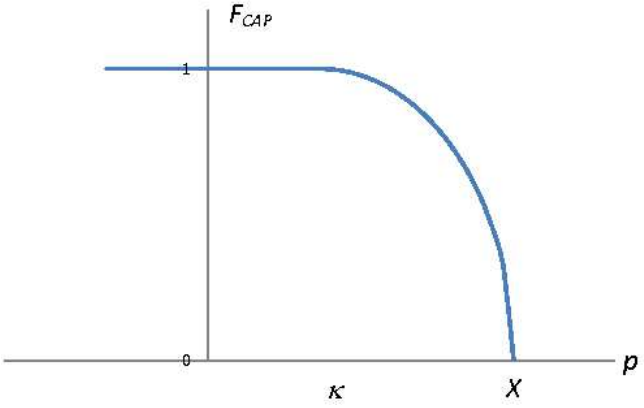


**Figure 3.2.** An elliptical cap function

initial shear modulus to the modulus after the elastic limit has been passed, the ratio between the compressive yield strength and the compressive ultimate strength, and the ratio between the tensile yield strength and the ultimate tensile strength.

Similar to the K&C model, third invariant dependence corresponding to a noncircular octahedral profile is obtained by using the Willam-Warnke function Eq. (1.7) as a scaling factor; see Fig.3.3. Unlike the K&C concrete model, where the ratio of a material tensile strength to compressive strength $\psi(p)$ is represented by a piecewise linear function, the RHT concrete model defines $\psi(p)$ as

$$\psi(p) = \psi_0 + BQ\frac{p}{f_c'}. \tag{3.3}$$

where $\psi_0$ is the tensile to compression meridian ratio, and $BQ$ is a brittle to ductile transition factor. By default, the model assigns a value of 0.6805 to $\psi_0$ and 0.0105 to $BQ$.

# Rate and scale dependence

The RHT model implements a strain rate law that uses a dynamic increase factor ($DIF$) for tension at varying strain rates. The $DIF$ is represented by a ratio of dynamic and static tensile strength,

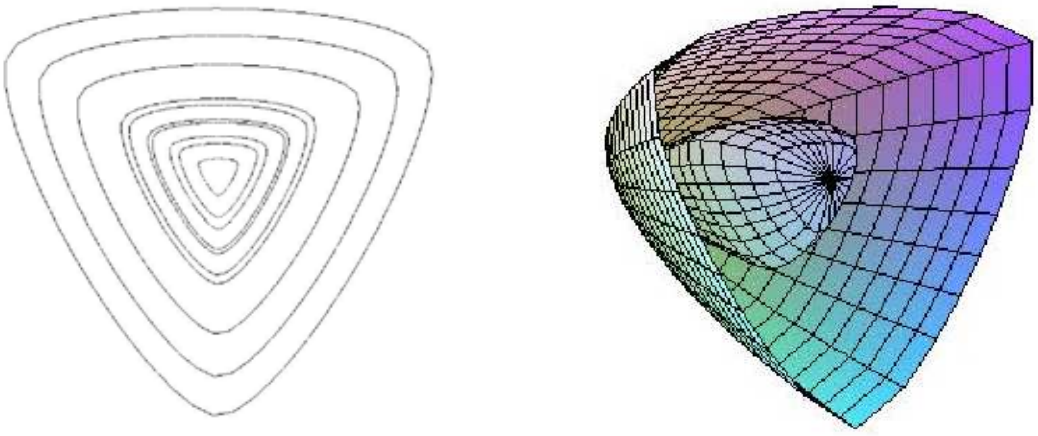

**Figure 3.3.** RHT octahedral profile and surfaces

and can be expressed as [35]

$$DIF = \frac{f_{ct}}{f_{cts}} = \begin{cases} \left(\frac{\dot{\varepsilon}}{\dot{\varepsilon}_s}\right)^{1.016\delta_s} & \text{for} \quad \dot{\varepsilon} \leq 30 \text{ s}^{-1}, \\ \beta_s \left(\frac{\dot{\varepsilon}}{\dot{\varepsilon}_s}\right)^{1/3} & \text{for} \quad \dot{\varepsilon} > 30 \text{ s}^{-1}, \end{cases} \tag{3.4}$$

$$\begin{aligned} \delta_s &= \frac{1}{10 + 6 f'_c / f'_{co}}, \quad \text{with} \quad f'_{co} = 10 \text{ MPa}, \\ \beta_s &= 10^{7.112\delta_s - 2.33}, \\ \dot{\varepsilon}_s &= 3 \times 10^{-6} \text{ s}^{-1}, \end{aligned} \tag{3.5}$$

where $f_{ct}$ is dynamic tensile strength at $\dot{\varepsilon}$, and $f_{cst}$ is the static tensile strength at a reference rate, $\dot{\varepsilon}_s$. The strain rate $\dot{\varepsilon}$ can be any value between $10^{-6}$ to 160 $\text{s}^{-1}$. The parameter $\delta_s$ is adjusted such that Eq. (3.4) approximates the *DIF* curve that complies with experimental data given in CEB-FIB Model Code [35], see Fig. 3.4.

For projectile and fragment impacts, cracking, spalling and scabbing are mainly influenced by the tensile strength, fracture energy, and strain rate in tension. Penetration, on the other hand, is influenced by the pressure and the strain rate in compression. When the sudden increase in strength occurs at lower strain rates, Unosson [37] pointed out that a scabbing in the simulation can be reduced by a using *DIF* value in tension. Hence, to predict the correct behavior of the penetration, spalling, and scabbing, *DIF* data for tension and compression are required.

The RHT model handles the scale effect similar to the K&C model, namely scaling of the fracture energy. A linear [19] or bilinear [16, 20] softening law, which is based on the crack opening, can be included in the RHT model post-failure response under tension [26] when the stress reduces to zero and the real crack is formed. The fracture energy $G_F$ and tensile strength $f_t$ are used to compute the crack width, $w_u$, as shown in Fig. 3.5. In the AUTODYN implementation

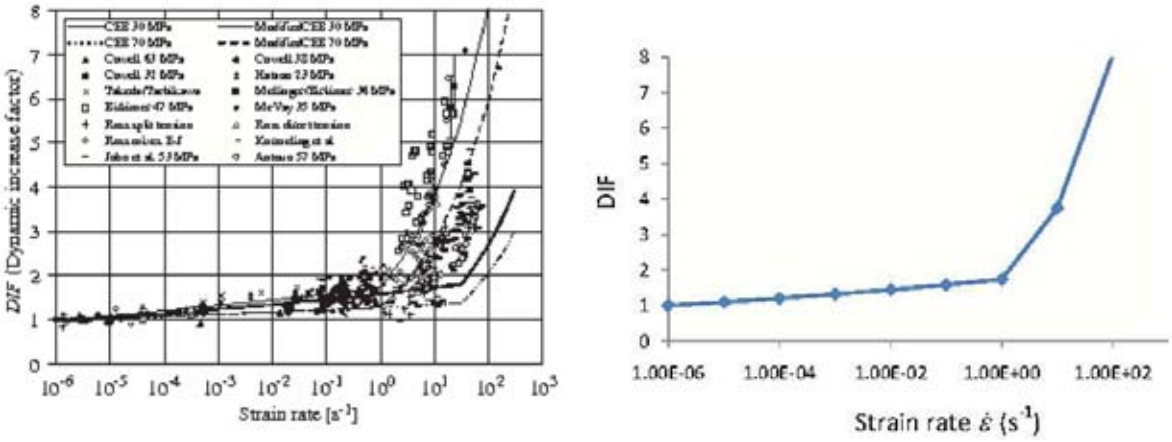


**Figure 3.4.** Left: Experimental data for *DIF* according to CEB-FIB design model code [26]. Right: *DIF* used in AUTODYN: RHT concrete model.

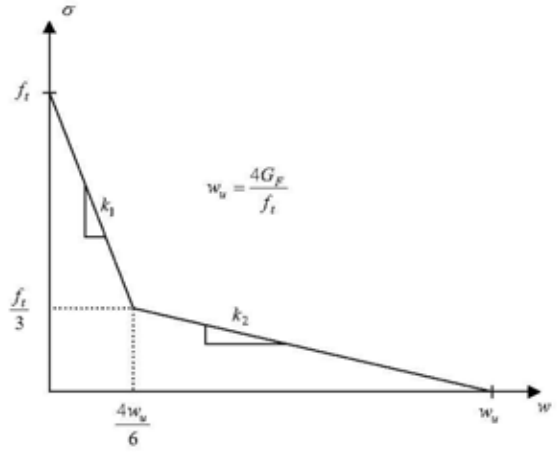


**Figure 3.5.** Bi-linear uniaxial stress-crack opening relationship

of the RHT model, the maximum cracking strain is related to the maximum crack opening using a smeared crack approach as

$$\varepsilon_u = \frac{w_u}{l} = \frac{4G_F}{f_t l}, \tag{3.6}$$

where $l$ is a characteristic length typically set equal to the cube root of element volume. The slopes in Fig. 3.5 are defined as

$$k_1 = \frac{f_t^2}{G_F} \quad \text{for} \quad \varepsilon \leq \frac{1}{6}\varepsilon_u, \tag{3.7}$$

$$k_2 = \frac{f_t^2}{10G_F} \quad \text{for} \quad \varepsilon > \frac{1}{6}\varepsilon_u, \tag{3.8}$$

where $\varepsilon$ is the cracking strain and $\varepsilon_u$ is the ultimate cracking strain. This approach is used when the erosion option is selected in AUTODYN. The implementation of the bilinear softening law to the RHT model is presented in [26]. In the current commercial release of AUTODYN, however, only a linear softening is available for the RHT concrete model. Its linear softening slope is defined as

$$k = \frac{f_t^2}{2G_F}. \tag{3.9}$$

# Damage accumulation

Once material begins to harden or soften, the damage factor $D$ is used to determine the value of the current strength surface. The damage factor is defined using

$$D = \sum \frac{\Delta\varepsilon^p}{\varepsilon^f}, \tag{3.10}$$

where $\Delta\varepsilon^p$ is the accumulated plastic strain, and $\varepsilon^f$ is the failure strain given by

$$\varepsilon^f = D_1 \left( \frac{p}{f_c'} - \frac{p_{spall}}{f_c'} \right)^{D_2}, \tag{3.11}$$

and parameters $D_1$ and $D_2$ are user input material constants. Damage causes a reduction in strength, hence, the strength surface is modified by shifting the surface from an initial surface to a current damage one. Similar to the K&C model, the current damaged surface during softening is interpolated between the limit and residual surfaces as

$$Y^* = (1-D)Y_m^* + DY_r^* \qquad \text{or} \qquad F(I_1) = (1-D)F(I_1)_m + DF_r(I_1), \tag{3.12}$$

and the residual surface is defined as

$$Y_r^* = a_{1f}\left(\frac{p}{f_c'}\right)^{a_{2f}} \quad \text{or} \quad F_r(I_1) = \frac{a_{1f}}{\sqrt{3}}\left(\frac{I_1}{3}\right)^{a_{2f}}, \tag{3.13}$$

$$\tag{3.14}$$

where

$a_{1f}$ = Initial slope of residual surface,
$a_{2f}$ = Residual strength exponent, pressure dependence for residual surface.

Equation (3.12) represents the interpolation between the undamaged material ($D = 0$) and damaged material ($D = 1$) at the limit surface.

# Plastic update

Similar to the K&C concrete models, a conventional regular associated flow rule is adopted by the RHT model. Therefore, the details on plastic update of this model is not covered in this report. The numerical schemes provided by the RHT model's developers can be found in [31].

# Shear and bulk moduli

Similar to the K&C model, the shear and bulk moduli are used and specified through the EOS provided by the host code(ANSYS AUTODYN). Several options are provided by ANSYS AUTODYN; for example, linear, polynomial, and $p-\alpha$ EOS. The bulk and shear moduli are controlled via the EOS similar to the K&C model. However, details on any form of modifications through scaling factors are not provided in the RHT or the ANSYS AUTODYN documentations.

# Chapter 4

# The BF1 GeoMaterial Model

The BF1 model is a version of the Sandia GeoModel [12] that has been enhanced to support softening. The BF1 softening model was originally designed to emulate and, where possible, enhance the softening approaches used in the Johnson-Holmquist ceramic models, JH1 and JH2 [21, 22]. Like the K&C and RHT models, the softening algorithm is based on strength reduction through collapse of the limit surface and a phenomenological damage reduction of elastic properties.

## Strength surfaces

Like the K&C and RHT models, the BF1 model uses three failure surfaces as shown in Fig. 2.1, and the corresponding yield criteria are

$$Y_y = \sqrt{J_2^\xi} = \frac{(F_m(I_1) - N)F_c(I_1,\kappa)}{\Gamma(\theta, I_1)}, \qquad \text{(yield surface)}, \tag{4.1}$$

$$Y_m = \sqrt{J_2^\xi} = \frac{F_m(I_1)}{\Gamma(\theta, I_1)}, \qquad \text{(limit surface)}, \tag{4.2}$$

$$Y_r = \sqrt{J_2^\xi} = \frac{F_r(I_1)}{\Gamma(\theta, I_1)}, \qquad \text{(residual surface)}, \tag{4.3}$$

where $F(I_1)$ is taken to be an affine-exponential spline:

$$F_m(I_1) = a_1 - a_3 \exp(-a_2 I_1) + a_4 I_1, \tag{4.4}$$

$$F_r(I_1) = a_{1f} - a_{3f} \exp(-a_{2f} I_1), \tag{4.5}$$

and $\xi = \mathbf{S} - \alpha$ is a shifted stress tensor ($\alpha$ is backstress).

Similar to the RHT model, the BF1 model provides an option for porosity effects, and the cap function is

$$F_c(I_1,\kappa) = \begin{cases} 1 & : \quad I_1 < \kappa, \\ 1 - \left(\frac{I_1 - \kappa}{X - \kappa}\right)^2 & : \quad \text{otherwise}, \end{cases} \tag{4.6}$$

In Eqs. (4.1)–(4.3), $J_2^{\xi}$ is the second invariant of the shifted stress (stress minus backstress) and $N$ is the maximum allowed translation of backstress. The BF1 limit surface is comparable to the K&C and RHT models, and the distance between the yield surface and the limit surface is controlled by the value $N$. For nonzero $N$, the motion of the yield surface towards the limit surface is accomplished by kinematic hardening, which accounts for the Baushinger effect and does not appear to be supported by the other two models.

Like the RHT model, the BF1 cap function $F_c(I_1, \kappa)$ accommodates material weakening caused by porosity. As in Fig. 3.2, the variable $\kappa$ marks the point where $F_c$ branches (smoothly) from a constant value of unity at low pressure to begin its descent along an elliptical path to the value zero at the hydrostatic compression elastic limit where the yield surface crosses the hydrostat at $I_1 = X$.

Like the K&C and RHT concrete model, the BF1 material model supports the Willam-Warnke $\Gamma(\theta)$ function for third invariant dependence, but it also provides Mohr-Coulomb and Gudehus options. The ratio $\psi(I_1)$ used in this model can be a constant or it can be determined automatically within the BF1 code as a pressure-dependent function coupled to pressure dependence of the TXC strength:

$$\psi(I_1) = \frac{1}{1 + \sqrt{3}A(I_1)}. \tag{4.7}$$

The ratio $\psi(I_1)$ is determined automatically based on the slope of the compressive meridian, $A(I_1)$. If this meridional slope is zero, then $\psi = 1$. The meridional slope steepens (with decreasing pressure) to a maximum allowed value. Thus, the yield surface smoothly varies from a von Mises character at high pressure to a maximum principal stress at low pressure. When used with the Willam-Warnke option, this gives the pressure varying octahedral profile similar to Fig. 2.2 and Fig. 3.3 for the K&C and RHT models, respectively.

Like the K&C and RHT models, the BF1 model allows the limit surface to collapse down to a residual surface as damage increases. Both the initial limit surface and residual surface are described using the form in Eq. (4.4). They merely use different $a-$parameters. The morphing of the limit surface between them as damage progresses relies on an internal alternative parameterization of Eq. (4.4). A limit surface of the form given in Eq. (4.4) can be viewed as bounded by the dashed lines in Fig. 4.1. The user specifies values for the indicated slopes residual surfaces, from which the code computes corresponding $a-$parameters.

As damage proceeds, each of the four limit surface parameters is interpolated linearly between intact and residual values. If for example, the user wishes to emulate a loss of hydrostatic tensile strength similar to the K&C model, then $PEAKI1$ for the residual surface is zero. To emulate damage similar to that of the Johnson-Holmquist damage (JH1 or JH2), the user would give reduced residual values for $FSLOPE$, $STREN$, and $PEAKI1$ (and $YSLOPE = 0$ for both intact and residual). In the absence of data for failed strength, the BF1 model defaults the residual strength parameters to that of sand ($PEAKI1 = 0$, $FSLOPE = 0.18$, $YSLOPE = 0$, $STREN$ = intact value).

An upcoming release of BF1 includes numerical efficiency enhancements that give 40% speed up by a return algorithm in a lower-dimensional space for which the result is then projected into

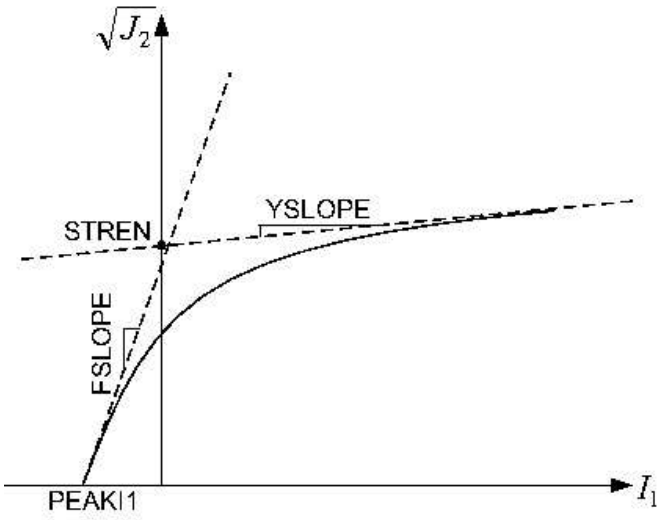


**Figure 4.1.** Parameters for residual surface

six dimensional space, similar to the approach of Bicanic and Pearce [3]. The new version also includes support for yield or limit surface vertices and new handling for pathological yield surface contours near the hydrostatic tensile limit.

# Rate and scale dependence

The plastic flow used by BF1 is rate dependent. Under high strain rates, elastic material response occurs almost instantaneously, but accumulated damage is retarded by the material's inherent "viscosity", which prohibits observable inelasticity to proceed instantaneously. Thus, at high rates, the material will appear to be more "elastic" than it would at low rates. Until sufficient time has elapsed for damage to accumulate, the stress will lie transiently outside the yield surface, or even outside the limit surface.

## Rate dependence

Unlike the K&C and RHT models that rely on *DIF* data to account for rate effect, the BF1 model uses a generalized Duvaut-Lions [10] rate-sensitive formulation, which computes two limiting solution for the updated stress:

1. the low-rate (quasi-static) solution $\sigma^L$ that is found by solving the rate-independent equations.

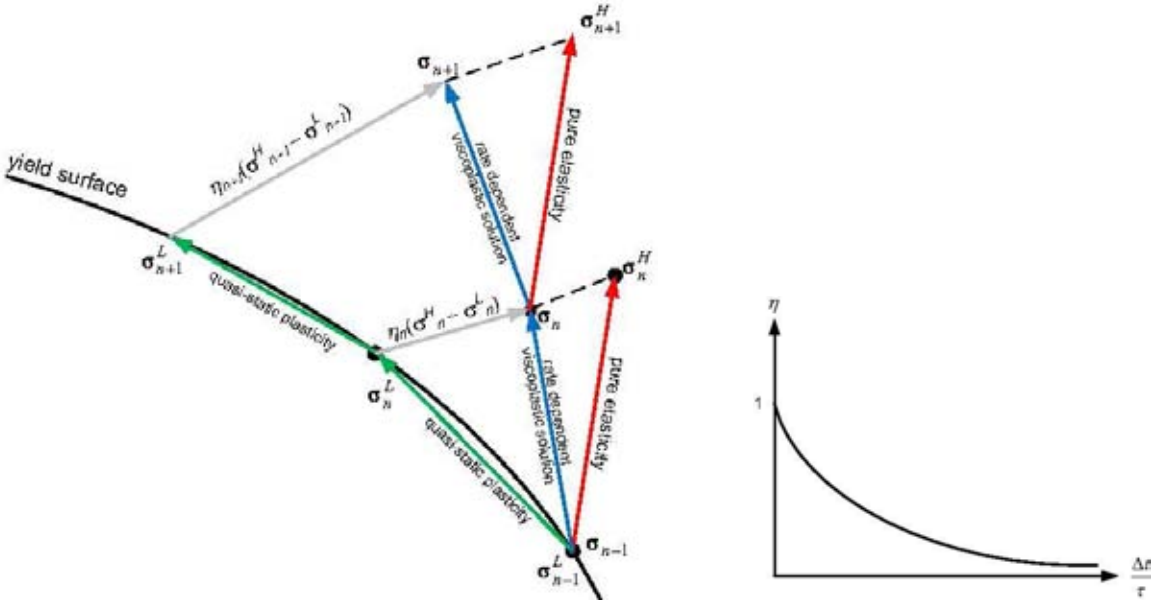


**Figure 4.2.** Illustrations of the generalized Duvaut-Lions rate sensitivity and the scale factor $\eta$ employed in the BF1 model [14]

2. the high-rate solution $\sigma_H$ corresponding to insufficient time for any plastic response to develop so that it is simply the trial elastic stress.

To a good approximation, as illustrated in Fig. 4.2, The Duvaut-Lions rate formulation updates stress using interpolation between the low-rate quasi-static plasticity solution $\sigma^L$ and the high-rate purely elastic solution $\sigma^H$,

$$\sigma \approx \sigma^L + \eta(\sigma^H - \sigma^L), \tag{4.8}$$

where $\eta$ is a scale factor that varies from 1 at high strain rates to 0 at low strain rates as shown in Fig. 4.2. To handle transients properly, the implementation in BF1 [12] is actually more sophisticated than Eq. (4.8).

The abscissa in Fig. 4.2 is normalized by the material's "characteristic" response time $\tau$. A time interval $\Delta t$ is considered "long" if $\Delta t \gg \tau$, and there is sufficient time for material to fully develop plastic response and yield a solution that coincides with the quasi-static solution $\sigma^L$. In contrast, the time interval is deemed "short" if $\Delta t \ll \tau$.

Like the K&C and RHT concrete models, which rely on the empirical *DIF* data, the BF1 also uses empirical data to provide flexibility in matching high strain rate for a wide range of material types. However, the similarity ends there. The dynamic increasing factor (*DIF*) that is used in the former models is a *function* of the strain rate, making it jump discontinuously if there is a jump in strain rate (as in the arrival of a shock). In the BF1 model, there is an effective

*DIF* that is a *functional* of the strain rate that corresponds to stress states that can lie outside the yield surface but cannot arrive or depart from such transient states instantaneously. In the BF1 formulation, experimental data for apparent increase in strength is interpreted as the steady state stress displaced from the yield surface under constant strain rate. The distinction between views is that the *DIF* function approach fails to capture the transients prior to reaching steady state. Moreover, the *DIF* function approach can cause numerical problems because it is capable of discontinuities. As detailed in the BF1 user's guide, the characteristic time is not a constant but instead may itself depend on the strain rate and on the position of the stress on the yield surface so that rate dependence of pore collapse can differ from that of cracking [5].

The BF1 model supports different levels of rate sensitivity depending on the mechanism of inelasticity. Specifically, pore collapse can be more rate sensitive than cracking, as has been observed in laboratory data [13, 5]. Rate dependence for softening is a relatively new addition to the BF1 model that is not documented in [12]. Softening is viewed as arising from crack growth. Since cracks tend to grow at a fixed speed regardless of the loading rate, BF1 treats softening rate dependence as a time-based process for which material scale effects enter naturally by recognizing that the amount of time required for a crack to propagate a fixed distance (e.g. the distance to the next crack to begin crack coalescence at the onset of catastrophic failure) must be itself fixed if crack speed is a constant. BF1 detects the onset of softening by stress reaching the limit surface, but it delays the subsequent degradation in elastic and strength properties until the required amount of time has passed. As mentioned, this delay time is viewed as the time needed to propagate a fixed distance and therefore its value is scale dependent.

Specifically, when the BF1 model is run with the BFS[1] enhancement, it is proportional to a characteristic length of the finite element similar to the one used by the K&C and RHT models. The BF1 model is used as a "base" damage model that is premised on the assumption that its material parameters have been assigned values appropriate to the scale of the finite element for a homogeneously deformed domain. As illustrated in Fig. 4.3, such tests ideally would be conducted for multiple specimen sizes to directly measure scale effects as well as inherent variability in measured properties. If $\bar{T}$ is the time-to-failure observed for a laboratory sample of volume $\bar{V}$, then the time-to-failure $T$ assigned to a finite element of volume $V$ is

$$T = \bar{T}\left(\frac{V}{\bar{V}}\right)^{1/3}. \tag{4.9}$$

One appeal of a time-based damage progression model is that it naturally leads to a dependence of the effective damage energy on loading rate. The amount of strain that can accumulated between $t_{\text{grow}} = 0$ and $t_{\text{grow}} = T$ is higher at high strain rates, thus leading to higher stresses, higher failure energy, and therefore an increase in the number of failed elements. This trend is consistent with fragmentation behavior observed in the laboratory where samples impacted at high rate produce a larger number of fragments than those impacted at low rates. This feature distinguishes BF1 from the K&C and RHT models, which apparently use rate insensitive fracture energies.

[1]The BFS model [5, 29] is a model for automatically assigning scale appropriate BF1 parameters based on the size of the finite element relative to the size of the specimen used in laboratory model calibration tests.

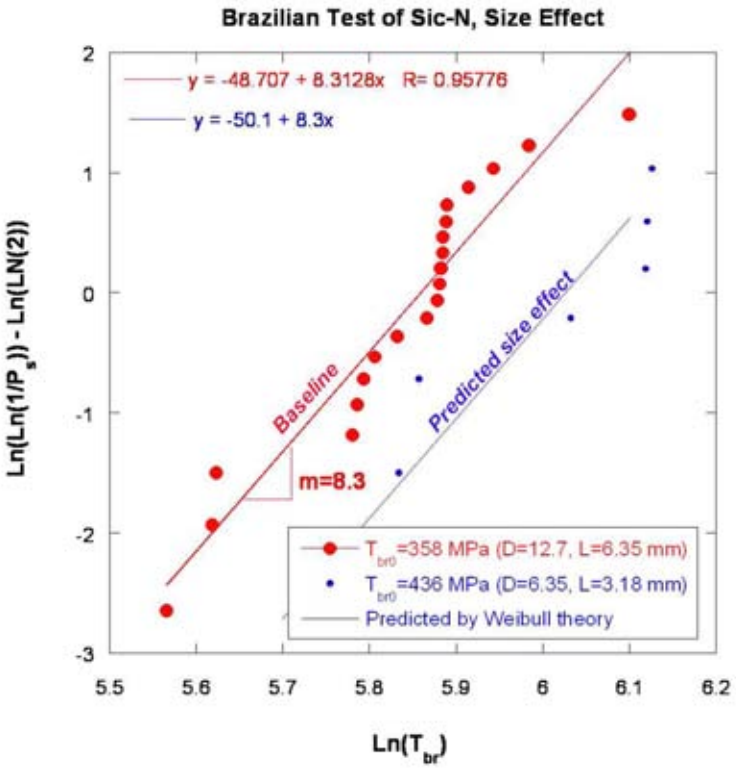


**Figure 4.3.** Standard Weibull distribution plots showing increased Brazilian strength $T_{br}$ with decreased sample size. Here, $P_s$ is the complementary cumulative probability, which may be interpreted as the probability that the sample is safe from failure. The slope of the fitted line is the Weibull modulus, which quantifies variability in strength.

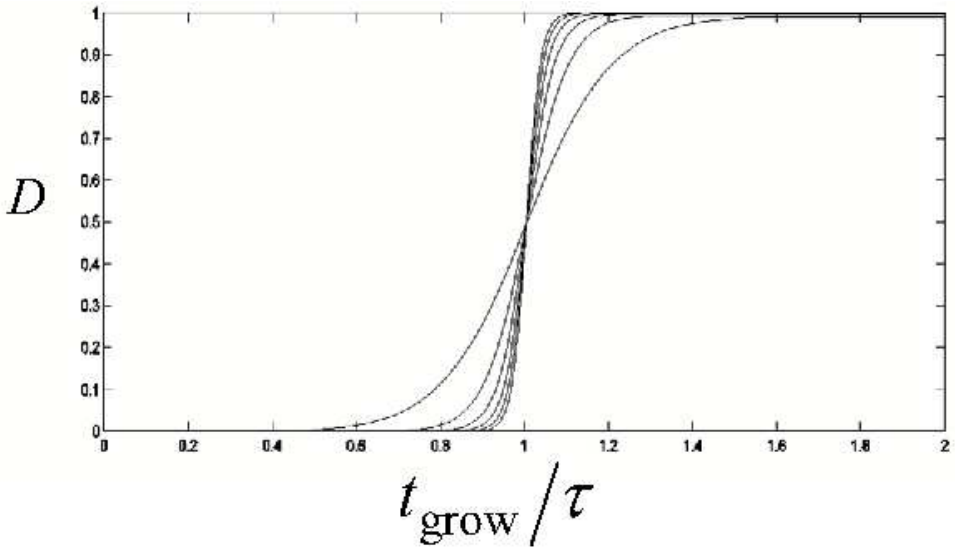


**Figure 4.4.** BF1 damage function for $FSPEED$ values in the range from 5 to 30. The higher $FSPEED$ values correspond to the steeper slope.

# Damage accumulation

During calculations, if the stress is at or above the limit stress, a time-of-growth variable is incremented as

$$t_{\text{grow}}^{n+1} = \Delta t, \tag{4.10}$$

where $\Delta t$ is the time step. Otherwise,

$$t_{\text{grow}}^{n+1} = t_{\text{grow}}^{n}. \tag{4.11}$$

Given the current value of $t_{\text{grow}}$, an adjustable phenomenological damage parameter is evaluated using a function of the form illustrated in Fig. 4.4.

The smoothness of the transition of damage from 0 to 1 is controlled by a user parameter $FSPEED$ such that large values of $FSPEED$ would correspond to a nearly step discontinuity from $D = 0$ to $D = 1$. The $FSPEED$ option was added merely as a convenience to allow BF1 to emulate the JH1 damage model [21] using large $FSPEED$ or JH2 [22] using smaller values of $FSPEED$ to allow more gradual development of damage.

Whereas many damage models might evolve damage as a function of accumulated plastic strain, the function in Fig. 4.4 evolves damage as a function of time. The rationale behind this choice is discussed below.

As damage progress from $D = 0$ to $D = 1$, the tangent shear and bulk moduli degrade from their initial values to residual values that are currently assigned internally in the code. Assuming that the residual state corresponds to a rubble-like state, the shear modulus is reduced to zero. The bulk modulus is reduced to a small fraction of its initial value if the pressure is tensile, but it equals its intact value if pressure is compressive. The reason why the tensile bulk modulus is not allowed to reach zero is not physical, but instead tied to the method for tracking of volumetric strain to detect recompression. This method is currently under revision to allow zero bulk modulus in tension.

The stiffness degradation component of the BF1 model is regarded by even its own developers as nothing more than an ad hoc means of achieving qualitatively correct behavior. A more physically based stiffness degradation model would allow development of induced anisotropy reflecting the tendency for quasi-brittle materials to develop orthotropically oriented cracks. Future revisions of BF1 are anticipated to support induced elastic anisotropy either by retrofitting its existing ability to model orthotropic rock joints or by introducing a directional damage theory based on the work of Dienes [9] and Kachanov [23]. At present, however, the shear modulus $G$ and bulk modulus $K$ are degraded as follows:

$$K = K^{\text{intact}}(1 - d_K), \tag{4.12}$$

$$G = G^{\text{intact}}(1 - d_G), \tag{4.13}$$

where

$$d_K = \begin{cases} 0 \quad \text{if} \quad p > 0 \quad \text{(compression)}, \\ D^* \text{ if} \quad p < 0 \quad \text{(tension)}, \end{cases} \tag{4.14}$$

and

$$d_G = D^* \frac{(dF/dI_1)_{p=p_{\text{current}}}}{(dF/dI_1)_{p=0}}. \tag{4.15}$$

The expression for $d_G$ is designed to allow full recovery of the shear stiffness as confining pressure increases. Recognizing from the work of Dienes [9] and Kachanov [23] that elastic compliance is related to the cube of crack size and recalling that crack propagation speeds tend to be constant, the $D^*$ used in the above formulas is based on the isotropic part of the anisotropic crack-degraded stiffness formulas of Dienes, and is expressed as

$$D^* = 1 - \frac{1}{1 + \left(\frac{1}{1-D} - 1\right)^3}. \tag{4.16}$$

Using $D^*$ instead of $D$ will cause the bulk modulus to "hang on" close to its initial value for a while to reflect the fact that small cracks do not significantly alter stiffness. A significant and sudden drop in stiffness can be seen only when cracks become large. As mentioned, the power of 3.0 dependence reflects trends predicted in microphysical theories for stiffness of a cracked body.

# Plastic update

During the initial hardening phase (before onset of damage) the BF1 model updates the material state using standard techniques of classical plasticity theory. As already mentioned, for example, the strain rate is decomposed into elastic and plastic parts, with the elastic part determined from elastic unloading data and the plastic part being a multiple of the flow potential gradient,

$$\dot{\varepsilon}^p = \dot{\mu}\left(\frac{\partial \phi}{\partial \sigma}\right), \tag{4.17}$$

where $\dot{\mu}$ is called the "consistency" parameter because its value is set to ensure consistency with the requirement that stress remain on the yield surface during plastic loading. The consistency parameter can be determined by satisfying

$$\dot{f} = \frac{\partial f}{\partial \sigma} : \dot{\sigma} + \frac{\partial f}{\partial \kappa}\dot{\kappa} + \frac{\partial f}{\partial \alpha} : \dot{\alpha} = 0. \tag{4.18}$$

Unlike the K&C and RHT models, the BF1 allows for kinematic hardening as well as isotropic hardening. As is typical in conventional plasticity modeling, closure of the governing equations (i.e. obtaining enough equations to solve, as detailed in [1]) requires specification of evolution equations for all internal variables. For BF1, there are two internal state variables: $\kappa$ for pore collapse and $\alpha$ for kinematic hardening.

The isotropic hardening is governed by the rate variable $\dot{\kappa}$, where $\kappa$ is the pressure at which void begins to collapse, see Fig. 3.2. The kinematic hardening is governed by $\dot{\alpha}$. It was shown in [12] that these rates are proportional to the consistency parameter and can be expressed as

$$\dot{\kappa} = h_k \dot{\mu} \qquad \text{and} \qquad \dot{\alpha} = \mathbf{H}_\alpha \dot{\mu}, \tag{4.19}$$

where $h_k$ is an isotropic hardening modulus, and $\mathbf{H}_\alpha$ is a kinematic hardening tensor, each of which is determined from laboratory data as described below.

## Evolution equation for pore collapse

If a material is capable of permanent volume change, then the material likely contains voids. Recall from Eq. (4.6) that the branch point $\kappa$ and the hydrostat intercept $X$ are used to characterize the effect of void collapse. The hydrostatic intercept $X_o$ equals the value of $I_1$ (which is proportional to pressure $p = I_1/3$) at which pores begin to collapse, as indicated by point A in Fig.4.5. There after, increasing pressure is required to continue pore collapse. If this pressure is provided, the yield hydrostat, $X = 3p$, intercept moves outward until all pores have been crushed out, at which

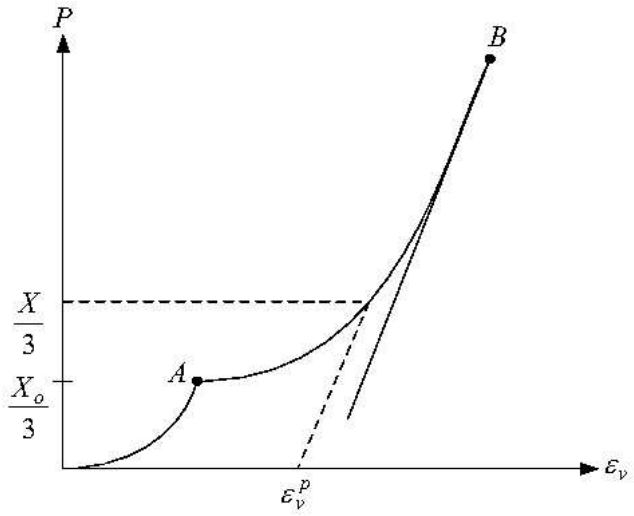


**Figure 4.5.** Hydrostatic pressure vs. volumetric strain

point the load and unload curves in hydrostatic compression become tangent, as indicated by point B in Fig. 4.5.

If the pressure is released at any point during hydrostatic compression, there will be permanent residual plastic volume change, $\varepsilon_v^p$, as labeled in Fig. 4.5. Thus, since a relationship between $X$ and $\varepsilon_v^p$ is directly measured in the laboratory, it might seem natural to use the hydrostat $X$ as an internal variable. However, for numerical reasons, it proves to be more convenient to use $\kappa$ as the internal state variable. Given the measured relationship between $X$ and $\varepsilon_v^p$ and the relationship between $\kappa$ and $X$ in Eq. (4.6), $\kappa$ and $\varepsilon_v^p$ are implicitly related. Then, by the chain rule

$$\dot{\kappa} = \frac{d\kappa}{d\varepsilon_v^p}\dot{\varepsilon}_v^p = \frac{d\kappa}{dX}\frac{dX}{d\varepsilon^p}\dot{\varepsilon}_v^p. \tag{4.20}$$

Moreover, since $\dot{\varepsilon}_v^p = \mathrm{tr}\dot{\varepsilon}^p$, Eq. (4.19) leads to

$$\dot{\kappa} = h_k\dot{\mu} \quad \text{where} \quad h_k = 3\frac{d\kappa}{dX}\frac{dX}{d\varepsilon_v^p}\frac{\partial\phi}{\partial I_1} \tag{4.21}$$

## Evolution equation for backstress

When kinematic hardening is enabled, a shifted stress tensor $\xi = \mathbf{S} - \alpha$ is used in the yield function instead of the actual stress. The backstress (deviatoric tensor) $\alpha$ is initially zero and evolves

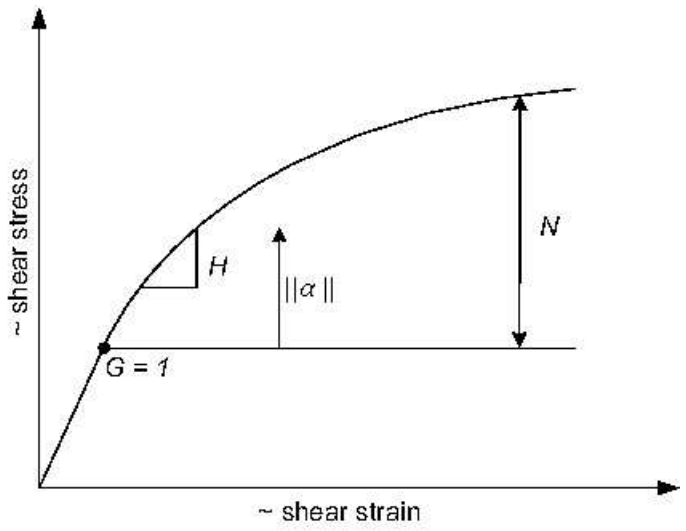


**Figure 4.6.** Qualitative sketch of shear stress vs. shear strain

proportionally to the deviatoric part of the plastic strain rate according to

$$\dot{\alpha} = HG^{\alpha}(\alpha)\dot{\gamma}^{p} \qquad \text{and} \qquad \dot{\gamma}^{p} = \text{dev}(\dot{\varepsilon}^{p}) = \left(\dot{\lambda}\frac{\partial\phi}{\partial\xi}\right), \tag{4.22}$$

where $H$ is a material constant and $G^{\alpha}(\alpha)$ is a scalar-valued decay function designed to limit the kinematic hardening such that $G^{\alpha} \to 0$ as second invariant of $\alpha$ approaches a user-specified maximum allowed value $N$. This behavior gives results similar to power law hardening as *qualitatively* illustrated in Fig. 4.6. The BF1 model uses the following decay function

$$G^{\alpha}(\alpha) = 1 - \frac{\sqrt{\text{tr}\alpha^{2}}}{\sqrt{2}N}. \tag{4.23}$$

Using Eqs. (4.19) and (4.22), the kinematic hardening modulus tensor is

$$\mathbf{H}_{\alpha} = HG^{\alpha}(\alpha)\text{dev}\left(\frac{\partial\phi}{\partial\xi}\right). \tag{4.24}$$

# Shear and bulk moduli

While the K&C model presumes a constant Poisson's ratio (from which nonlinear shear modulus can be computed from nonlinear bulk modulus), the BF1 model computes the shear and bulk

modulus using input parameters that are obtained by curve fitting hydrostatic and triaxial data to nonlinear functions. The BF1 model supports linear and nonlinear hypoelasticity. Unlike the K&C and RHT model, where tabulated data are used, the nonlinear elasticity in BF1 is implemented by allowing the tangent moduli to vary with the stress according to

$$K = b_0 + b_1 \exp\left(-\frac{b_2}{|I_1|}\right), \tag{4.25}$$

$$G = g_0 \left[\frac{1 - g_1 \exp\left(-g_2 J_2^{1/2}\right)}{1 - g_1}\right], \tag{4.26}$$

where $b_0, b_1, g_0, g_1$ and $g_2$ are material parameters fitted to experimental data. The model is linear elastic if $b_0$ and $g_0$ are specified, and all other elastic parameters are zero (or unspecified). Unlike the K&C and RHT models, additional terms (with additional parameters) are available to support elastic-plastic coupling, where plastic hardening changes elastic properties (e.g. pore collapse induces elastic stiffening).

A disadvantage of Eqs. (4.25) and (4.26) is that they are difficult to parameterize because neither is integratable to obtain a closed form analytical expression for stress as a function of elastic strain. Alternatives are therefore under investigation. Other concerns are that Eqs. (4.25) and (4.26) have not been well validated in tension, and the current (2008) implementation does not consistently incorporate a "z-tensor" of the type discussed by Brannon [14] that is required in incremental plasticity with elastic-plastic coupling.

Like the K&C and RHT models, BF1 uses an isotropic elastic stiffness except that some pre-existing initial elastic anisotropy is optionally available for joints. However, since damage generally *induces* significant anisotropy in stiffness, all three models currently rely on very fine meshing so that deformation-induced anisotropy is approximated through explicit (mesh resolved) heterogeneity.

# Chapter 5

# LS-DYNA Concrete Model 159 (CSCM)

This chapter presents an additional overview of a new concrete material found in LS-DYNA, Concrete Model 159 (referred to as CSCM in this report). It was developed for DYNA3D Analysis Tools for Roadside Safety Applications II (2007) program by the U.S. Department of Transportation [11]. Since this model is not a part of this survey project's original Statement of Work (SOW), only a brief summary of its features will be given here.

## Strength surfaces

The CSCM model uses strength surfaces similar to the previous models investigated in this report. The failure surface is defined by the three invariants together with the cap hardening parameter similarly to the RHT and BF1 models. The yield function is expressed by

$$f(I_1, J_2, J_3, \kappa) = J_2 - \Gamma(\theta, I_1) F_f^2 F_c \tag{5.1}$$

where $\Gamma(\theta, I_1)$ is the Rubin third-invariant factor. The cap function is the same as in the RHT and BF1 models (see Chapters 3 and 4). The same affine-exponential spline used by the BF1 model is used to describe the limit surface,

$$F_m(I_1) = a_1 - a_3 \exp^{-a_2 I_1} + a_4 I_1 \tag{5.2}$$

The initial yield stress is then determined from the limit surface using

$$F_y(I_1) = N_H(a_1 - a_3 \exp^{-a_2 I_1} + a_4 I_1) \tag{5.3}$$

where $N_H$ is a factor ranging between $0.7 < N_H \leq 1$, which governs the location of the initial yield surface. Therefore, the CSCM model is similar to the RHT model's use of a multiplier to specify the separation between the initial yield surface, whereas the BF1 model specifies this separation additively.

The CSCM model supports kinematic hardening very similar to the BF1 model. The translation of the yield surface is done via the back stress $\alpha$. The total stress is updated by summing the initial

stress and the backstress. The hardening rule used by this material model is based on stress to ensure that the shear surface coincides with the limit surface. The rate of kinematic hardening is controlled by a user input $C_H$, and the incremental back stress is expressed as

$$\Delta\alpha = C_H G(\alpha)(\sigma - \alpha)\Delta\dot{\varepsilon}\Delta t. \tag{5.4}$$

The quantity $G(\alpha)$ is used to limit the increment such that the yield surface cannot move beyond the limit surface as discussed in Chapter 4 for the BF1 model. In fact, the above equation can be compared with Eq. (4.78) in [12]. No simulations were performed to determine if the CSCM kinematic hardening model is identical to the BF1 model in all respects.

# Rate and scale dependence

The strength of the model is increased with increasing strain rate. The CSCM model applies rate effects to the limit surface, residual surface, and the fracture energy as shown in the previous sections. A modified Duvaut-Lions formulation is applied to the yield surface such that the high-rate stress is an interpolation between the quasistatic low-rate stress and the elastic stress:

$$\sigma \approx \sigma^L + \eta(\sigma^H - \sigma^L), \quad \text{where} \quad \eta = \frac{\Delta t/\gamma}{1 + \Delta t/\gamma}. \tag{5.5}$$

A similar equation is given in the BF1 model's introduction to rate dependence, but the BF1 documentation points out that additional terms are needed once the dynamic stress lies outside the quasistatic yield surface.

As discussed in Chapter 4, the viscoplastic stress is bounded between the current rate-independent stress and the elastic trial stress at each time step. The high strain rate is handled by modifying $\gamma$ using

$$\gamma = \frac{\gamma_o}{\dot{\varepsilon}^n} \tag{5.6}$$

Equation (5.6) allows for user input parameters, $\gamma_o$ and $n$, that can fit rate effects data at high and low strain rates. These parameters are used to represent *DIF* specifications given by CEB [35] similar to the K&C and RHT models. Input parameter $\gamma$ can be determined using the following relationships as given in CEB-FIP [35],

- Tension:

$$DIF = \begin{cases} \frac{\dot{\varepsilon}}{\dot{\varepsilon}_o}^{1.016\delta_s} & \text{for } \dot{\varepsilon} \leq 30\text{s}^{-1} \\ \beta_s \frac{\dot{\varepsilon}}{\dot{\varepsilon}_o}^{1/3} & \text{for } \dot{\varepsilon} > 30\text{s}^{-1}, \end{cases} \tag{5.7}$$

where

$$\begin{aligned}
\delta_s &= \frac{1}{10+6f_c'/f_co}, \\
\log\beta_s &= 7.112\delta_s - 2.33, \\
f_co &= 10\text{ MPa}, \\
\dot{\varepsilon}_o &= 30\times10^{-6}\text{s}^{-1}, \text{ and} \\
f_c' &= \text{ concrete compressive strength.}
\end{aligned}$$

- Compression:

$$DIF = \begin{cases} \frac{\dot{\varepsilon}}{\dot{\varepsilon}_o}^{1.026\alpha_s} & \text{for } \dot{\varepsilon} \le 30\text{s}^{-1} \\ \beta_s \frac{\dot{\varepsilon}}{\dot{\varepsilon}_o}^{1/3} & \text{for } \dot{\varepsilon} > 30\text{s}^{-1}, \end{cases} \tag{5.8}$$

where

$$\begin{aligned}
\alpha_s &= \frac{1}{5+9f_c'/f_co} \\
\log\gamma_s &= 6.156\alpha_s - 2, \\
\dot{\varepsilon}_o &= 30\times10^{-6}\text{s}^{-1}, \text{ and} \\
f_c' &= \text{ concrete compressive strength.}
\end{aligned}$$

Despite having a similar base-line formulation to handle the rate effect as the BF1 model (using Duvuat-Lions rate sensitivity formula), the CSCM model has a built-in feature that allows a user to include DIF data for the rate effect. In addition, a user is also given an option to apply the DIF to the static fracture energy (enabled by the model's defaults), which causes the fracture energy to be strain rate dependent. The CSCM model's default DIF is based on the developer's experience, and is different from those given in CEB-FIP model code.

Similar to the K&C and RHT models, the CSCM model handles scale effects by incorporating an element characteristic length $w_u$ (cube root of the element volume). The model calculates the damage parameters as a function of element size. Regardless of element size, the fracture energy, $G_f$, remains constant. The fracture energy is regulated separately between brittle and ductile softening, and is computed by integrating the stress-displacement curve.

$$G_f = \begin{cases} r_{0b}w\left(\frac{1+b}{ab}\right)\log(1+b) & \text{for brittle softening} \\ 2r_{0d}w\left(\frac{1+d}{cd}\right)\log(1+d) + 2w\left(\frac{1+d}{c^2}\right)\int_0^\infty \frac{ye^{-y}}{1+ce^{-y}}dy & \text{for ductile softening,} \end{cases} \tag{5.9}$$

where

$$\begin{aligned}
y &= -c\left(\sqrt{x}-\sqrt{x_o}\right)\sqrt{\frac{f'}{w}}, \\
x &= \text{displacement,} \\
x_o &= \text{displacement at peak strength } f'.
\end{aligned}$$

Using Eqs. (5.10) and (5.9), the softening parameters $a$ and $c$ are computed according to the element characteristic length $w$, while $b$ and $c$ remain user input parameters. The value $G_f$ is approximated by the model from three fracture energy inputs: (1) from tensile stress, $G_{ft}$, (2) shear stress, $G_{fs}$, and (3) compressive stress, $G_{fc}$. When rate effects are considered, the fracture energy is scaled using

$$G_f^{vp} = G_f \left( \frac{r_o}{r_s} \right)^n. \tag{5.10}$$

The range of $0.5 \leq n \leq 1$ is recommended by the developer. When $n$ equals to 1, the $G_f^{vp}$ is proportional to the increase in strength with rate effects.

# Damage accumulation

Both strain softening and modulus reduction are accounted for in the damage formulation based on [34]. The damage stress, $\sigma^d$, is computed by

$$\sigma^d = (1-D)\sigma^{vp} \tag{5.11}$$

where $D$ is a damage parameter ranging from 0 to 1, and $\sigma^{vp}$ is a stress tensor without damage, which is updated from the viscoplasticity algorithm. This algorithm structure of applying damage after evaluation of the non-damaged stress update is identical to what was used in the versions of the BF1 model predating 2008. (Starting in 2008, the damage part of the BF1 algorithm was integrated within the stress update subcycles.)

The CSCM model handles damage using a strain-based energy approach. When this energy exceeds a material damage threshold, damage is initiated and accumulated via the parameter $D$. The damage threshold is determined using two different formulations for brittle and ductile damage. Unlike the BF1 model, which allows damage in compression, brittle damage accumulates in the CSCM model only when the pressure is tensile. Its damage threshold, $\tau_b$, depends on the maximum principal strain

$$\tau_b = \sqrt{E\varepsilon_{\max}^2}. \tag{5.12}$$

The brittle damage initiates when $\tau_b > r_{0b}$, where $r_{0b}$ is the initial brittle damage threshold. Such behavior is supported as a special case in the BF1 model.

Ductile damage, on the other hand, accumulates when the pressure is compressive, and the damage threshold, $\tau_d$ depends on the total strain components and is expressed as

$$\tau_d = \sqrt{\frac{1}{2}\sigma : \varepsilon}. \tag{5.13}$$

It initiates when the initial ductile damage threshold, $r_{0d}$, is exceeded.

The rate effect is accounted for by shifting the damage threshold using

$$r_0 = \left(1 + \frac{E\dot{\varepsilon}\gamma}{r_s\sqrt{E}}\right) r_s, \tag{5.14}$$

where $r_o$ is the shifted threshold with viscoplasticity, $r_s$ is the damage threshold before the application of viscoplasticity, and $\gamma$ is rate effects. The shifted damage threshold allows the delay of the damage initiation while the plasticity accumulates. This approach appears to be unrelated to the damage delay strategies of the other three models.

Damage accumulation during softening is computed as a function of the damage threshold using

$$D(\tau) = \begin{cases} \frac{0.999}{b}\left(\frac{1+b}{1+b\exp^{-a(\tau-r_{0b})}} - 1\right) & \text{for brittle } \tau = \tau_b, \\ \frac{D_{\max}}{d}\left(\frac{1+d}{1+d\exp^{-c(\tau-r_{0d})}} - 1\right) & \text{for ductile } \tau = \tau_d \end{cases} \tag{5.15}$$

The parameters $a, b, c$, and $d$ are determined by curve-fitting Eq. (5.15) to the softening portion of a stress-strain plot. The parameter $D_{\max}$ represent a maximum attainable damage and is defined as

$$D_{\max} = \begin{cases} \left(\frac{\sqrt{3J_2}}{I_1}\right)^{1.5} & \text{if } \frac{\sqrt{3J_2}}{I_1} < 1 \\ 1 & \text{if otherwise.} \end{cases} \tag{5.16}$$

When considering rate effects, the above equation is scaled using

$$D_{\max} = D_{\max} \times \max\left[1, \left(1 + \frac{r_0}{r_s}\right)^{1.5}\right] \tag{5.17}$$

In the current release of the CSCM material model, the exponent 1.5 is set internally by the developer based on examination of single element simulations. The maximum increment of the damage in a single time step is 0.1, and it is also set internally by the model.

Incidentally, Eq. (5.15) allows flexibility in the damage accumulation behavior that is similar to the time-based approach used in the BF1 model.

# Plastic update

Similar to the other concrete models, a conventional regular associated flow rule is adopted by the CSCM model. Therefore, the details on plastic update of this model are not covered in this

report. According to the developers, the model efficiency is improved by using subincrementation instead of iteration to return the stress state to the yield surface. It is invoked only when the current strain increment exceeds a maximum strain limit specified by a user or the model's default. The numerical schemes provided by the CSCM model's developers can be found in [30, 32].

## Shear and bulk moduli

The CSCM model computes the default shear and bulk moduli using

$$G = \frac{E}{2(1+\nu)} \qquad \text{and} \qquad K = \frac{E}{3(1-2\nu)}, \tag{5.18}$$

where $E$ is the Young's modulus and $\nu$ is the Possion's ratio. The Young's modulus $E$ is determined from an equation in CEB-FIP:

$$E = E_C \left( \frac{f_c'}{10} \right)^{1/3}, \tag{5.19}$$

where $E_C$ is the Young's modulus of a 10 MPa concrete. The Young's modulus $E_C$ is not used in the prepeak hardening part of the simulations.

# Chapter 6

# Model comparisons

This chapter presents a list of the comparison of theory and implementation of each model. In addition, the four models are also compared numerically for several case studies.

## Comparison of theory and implementation

Listed below are the features comparison of each model:

- The K&C concrete model relies most heavily on a set of empirically obtained data and curves. The accuracy of the result depends on a good set of data for yield stress factor $\eta$ and effective plastic strain $\lambda$, which are obtained via trial and error.
- The RHT, BF1, and CSCM models support a cap on the yield surface, while the K&C model does not appear to have this option (although the K&C model does allow porosity effects in the compaction EOS).
- The BF1 model supports intrinsic anisotropy through an elastic joint model. The CSCM model supports intrinsic elastic anisotropy associated with rebar. Both BF1 and CSCM models support deformation induced anisotropy thru kinematic hardening. None of the other models support anisotropy in any form. All of these models, including the BF1 and CSCM models, neglect the anisotropy that one might expect from oriented crack growth.
- The BF1 model determines the TXE/TXC strength ratio $\psi$ automatically based on the slope of the compressive meridian. If this slope is zero, $\psi = 1$. As the slope increases to a maximum allowed value (corresponding to a principal stress criterion), $\psi = 1/2$. The RHT model appears to be handling this issue in a similar manner. On the other hand, the K&C model defines $\psi$ as a piecewise function of pressure, where $\psi$ is always $1/2$ in the tensile pressure range.
- All four models offer defaults for unspecified parameters. The K&C model defaults values to that for 45MPa concrete. The RHT model offers defaults via loading preset parameters for 35MPa and 140MPa concretes. The BF1 model offers preset parameters for 23MPa concrete and conventional strength Portland cement as well as several other materials such as limestone and ceramic. Moreover, when building a new parameter set from scratch, the BF1

model defaults to reasonable guesses. For example, if no flow parameters are given, they default to associative flow parameters. The CSCM model automatically generates parameters for concretes having strengths that range between 20 and 58 MPa via built in quadratic fitting equations.

- Softening is best handled in the BF1 model by using it in combination with statistical heterogeneity and scale effects available in the BFS enhancement that can be regarded as an add-on available only in certain host codes. The K&C, RHT, and CSCM models appear to use only scale effects, but they could be modified to be run with statistics as well if they use an input parameter change of variables similar to the BF1 model use of the parameters in Fig. 4.1 as alternatives to its $a$-parameters. Parameter re-definition is needed when running with uncertainty to ensure that admissible realizations of the failure surfaces are generated.

- The K&C, RHT, and CSCM models deal mainly with concrete material, and may seem to require fewer user input parameters than the BF1 model, but this seems to be simply because parameters for those models default to concrete values. The greater concern is that some built-in parameters (i.e., not controllable by the user) may limit usefulness of the K&C and RHT models for other concrete-like materials such as rocks.

  Although the BF1 model has many possible user input parameters, it automatically sets defaults for any unspecified parameters. The BF1 model might be capable of simulating responses of a wider range of materials. For example, user input parameters can be modified to model simpler elastic materials, as well as classical plasticity idealizations such as von Mises, Tresca, and Mohr-Coulomb theories. The ability to reduce to simpler models has allowed the BF1 model's solution algorithm to be rigorously tested against analytical solutions.

- To model rate sensitivity, the K&C, RHT and CSCM models use a strength enhancement factor (or $DIF$), which follows the concrete data given in CEB-FIP design code. The K&C model allows for data of $DIF$ to be entered in a tabulated form. The RHT model, on the other hand, cannot cover the whole range of strain rate given in CEB-FIP because it represents $DIF$ vs. $\log\dot{\varepsilon}$ only in a linear form.

  Both BF1 and CSCM models handle rate effects using a Duvaut-Lions overstress formulation that is time based rather than strain rate based, which therefore allows for more accurate prediction of transients. These models incorporate a characteristic material response time. The CSCM model includes a means of setting the response time to match CEB-FIP data, whereas no automated support is currently available in the BF1 model to match specified data for rate effects in uniaxial strain loading.

- Both K&C and RHT models support user-specified EOS. The RHT supports a wide range of EOS forms that includes linear, polynomial, $p-\alpha$, and user tabulated compaction data, etc. The K&C models allow EOS to be specified only in a tabulated form. On the other hand, the BF1 and CSCM models provides a built-in nonlinear EOS designed to match data over pressure ranges ordinarily encountered in low to moderate pressure hydrostatics tests, and does not allow for any user specified EOS methods.

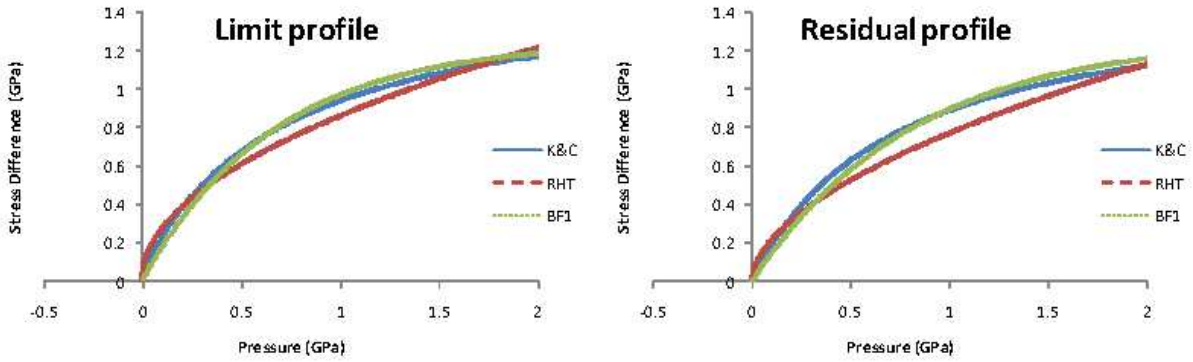


**Figure 6.1.** Comparison of meridian profiles to the K&C's profile. (The CSCM and BF1 curves coincide.)

- The BF1 model includes elastic-plastic and elastic-damage coupling (plasticity or damage changes the bulk modulus). The K&C model has no coupling of elastic properties to inelastic loading history. However, it scales the bulk modulus depending on pressure using a scaling factor. The coupling feature is unclear for the RHT model because this information is lacking in its user manual. All three models support nonlinear bulk modulus.

- The K&C, BF1, and CSCM models provide well-documented user manuals (in English), which also explain the schemes used in detail. On the other hand, the user manual for the RHT model is not available with the packaged model.

# Numerical comparison

The data used for the RHT, BF1, and CSCM models are tuned to yield results similar to those presented by Unosson [37] using the K&C model . The material models' default values are used for the parameters when their input information are insufficient. This section refers to the user's inputs using symbols given in AUTODYN and LS-DYNA [6, 27].

## Meridional profile

This section presents a numerical comparison of the meridional curves obtained from the four investigated models. The curves from the RHT, BF1, and CSCM models are constructed based on the parameters for the 153MPa concrete used for the K&C model in [37]. These parameters are shown in Table 6.1. The comparisons of the curves from each model are shown in Fig.6.1.

**Table 6.1.** Parameters for meridional curves

| Model | parameters | value |
|---|---|---|
| All | Compressive strength, $f_c'$ | 153 MPa |
| All | Tensile strength, $f_t$ | 8.2 MPa |
| K&C | limit surface parameter, $a_0$ | 50.6 MPa |
| K&C | limit surface parameter, $a_1$ | 0.465 |
| K&C | limit surface parameter, $a_2$ | 65.7 GPa$^{-1}$ |
| K&C | residual surface parameter, $a_{0f}$ | 0.0 MPa |
| K&C | residual surface parameter, $a_{1f}$ | 0.465 |
| K&C | residual surface parameter, $a_{2f}$ | 65.7 GPa$^{-1}$ |
| RHT | limit surface initial slope, $A$ | 2.2 |
| RHT | limit surface exponent, $N$ | 0.5 |
| RHT | residual surface initial slope, $B$ | 1.8 |
| RHT | residual surface exponent, $M$ | 0.55 |
| BF1 | limit surface parameter, $a_1$ | 722 MPa |
| BF1 | limit surface parameter, $a_2$ | $4.99 \times 10^{-10}$ |
| BF1 | limit surface parameter, $a_3$ | 713 MPa |
| BF1 | limit surface parameter, $a_4$ | none |
| BF1 | limit surface parameter, $FSLOPEI$ | 0.36 |
| BF1 | limit surface parameter, $STRENI$ | 722 MPa |
| BF1 | limit surface parameter, $PEAKI1I$ | 24.6 MPa |
| BF1 | residual surface parameter, $FSLOPEF$ | 0.3 |
| BF1 | residual surface parameter, $STRENF$ | 733 MPa |
| BF1 | residual surface parameter, $PEAKI1F$ | 246 Pa |
| CSCM | limit surface parameter, $\alpha$ | 722 MPa |
| CSCM | limit surface parameter, $\beta$ | $4.99 \times 10^{-10}$ |
| CSCM | limit surface parameter, $\lambda$ | 713 MPa |
| CSCM | limit surface parameter, $\theta$ | none |

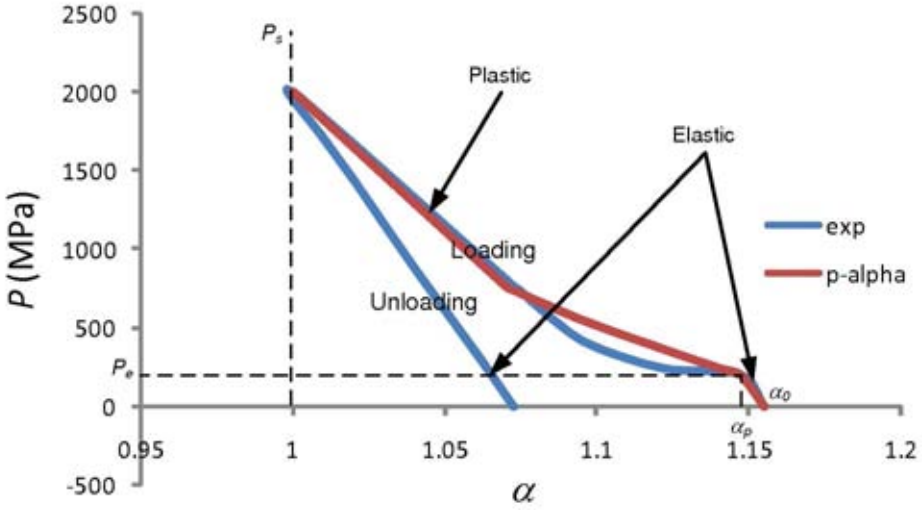


**Figure 6.2.** $p-\alpha$ equation of state employed by the RHT model.

**Table 6.2.** $P-\alpha$ EOS input parameters

| Input parameters | values |
|---|---|
| Porous density (kg/m$^3$), $\rho_p$ | 2572 |
| Porous sound speed (m/s), $c_p$ | 3200 |
| Initial compaction pressure (MPa), $p_e$ | 200 |
| Solid compaction pressure (MPa), $p_s$ | 2000 |
| Compaction exponent, $n$ | 2 |
| Bulk modulus (GPa), $K$ | 28.43 |

## Single element test: isotropic compression

Single element isotropic compression tests are conducted for each model, and hydrostatic pressure versus volumetric strain are obtained. The results are compared to the experimental data for a 153MPa concrete provided in [37]. Both K&C and RHT models require the EOS's to be specified. The K&C model requires a tabular EOS. The RHT model provides options for various functional forms of the EOS. For porosity effects, our test simulations employ the following $p-\alpha$ model:

$$\alpha = 1 + (\alpha_p - 1)\left[\frac{p_s - p}{p_s - p_e}\right]^n. \tag{6.1}$$

The parameters $\alpha_p, p_s$ and $p_e$ used here are defined and shown in Fig. 6.2 and Table 6.2.

The BF1 and CSCM models have built-in mechanical EOS and they both employ the following relationship between porosity and plastic volumetric strain (which is an indirect measure of pore

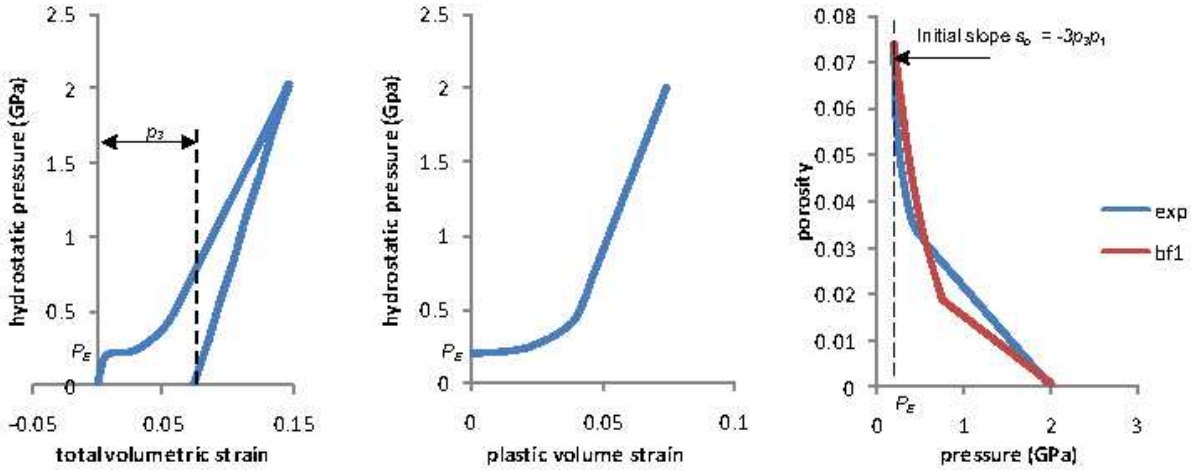


**Figure 6.3.** Equation of state: BF1 and CSCM crush curve

**Table 6.3.** Uniaxial strain loading for single element tests

| time (s) | displacement (m) K&C, BF1, CSCM | velocity (m/s) RHT |
|---|---|---|
| 0.0 | 0.0 | -0.3 |
| 1.0 | -0.3 | -0.3 |
| 1.000001 | - | 0.3 |
| 2.0 | 0.0 | 0.3 |

collapse):

$$p_3 - \bar{\varepsilon}_v^p = p_3 e^{-(p_1+p_2\bar{\xi})\bar{\xi}}, \quad \text{where} \quad \bar{\xi} = \bar{X} - \bar{p}_0 = 3(p - P_E). \tag{6.2}$$

The parameters $p_1, p_2, p_3$ and $P_E$ are defined in Fig. 6.3. The parameters required by the RHT $p-\alpha$, BF1 and CSCM crush curves are approximated by curve fitting the EOS data given in [37] to the K&C model. The comparison of the hydrostatic compression curves from each model is illustrated in Fig. 6.4

## Single element test: uniaxial strain

Single element uniaxial strain tests are conducted using the data shown in Tables 6.1 and 6.4. The loading data for each model are given in Table 6.3. Figure 6.5 shows a comparison of the stress difference $\sqrt{3J_2}$ versus pressure. All of the material models show similar behavior except the K&C model. In this test, the pressure exceeds the maximum pressure data given in the EOS table used

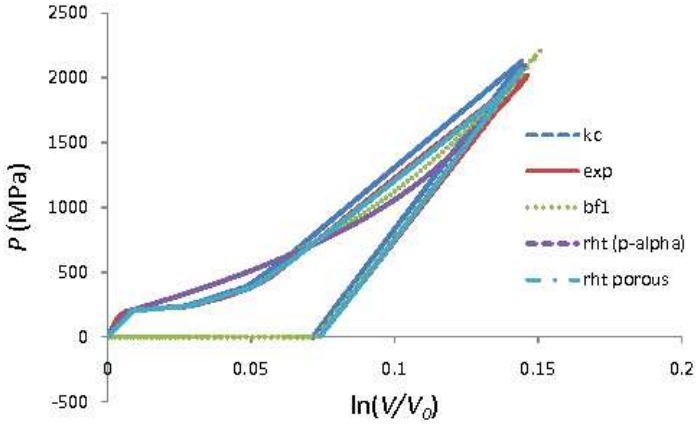


**Figure 6.4.** Comparison of hydrostatic pressure versus volumetric strain

**Table 6.4.** Material properties for concrete

| Property | value |
|---|---|
| Density (kg/m$^3$) | 2770 |
| Uniaxial compressive strength (MPa) | 153 |
| Modulus of elasticity (GPa) | 58 |
| Poisson's ratio | 0.16 |
| Bulk modulus (GPa) | 28.4 |
| Shear modulus (GPa) | 25 |

by the K&C model, and extrapolated data are added to the EOS table for the K&C model to obtain results beyond 2 GPa.

## Projectile penetration

Here we present numerical simulations of the perforation of a high performance concrete with a 75 mm steel projectile using the RHT and CSCM material models. The goal of these simulations is to investigate the results obtained using these two models and to compare them to the results from the K&C model given in [37]. ANSYS: AUTODYN is used for the investigation of the RHT concrete model, while LS-DYNA is used for the CSCM model. The data used in the RHT and CSCM models are tuned to give similar results to Unosson's as discussed in the single elements sections. These data are shown in Tables 6.5 - 6.7. A simplified Johnson-Cook strength model is used for the steel projectile to ensure that the pressure in the target concrete does not damage the projectile.

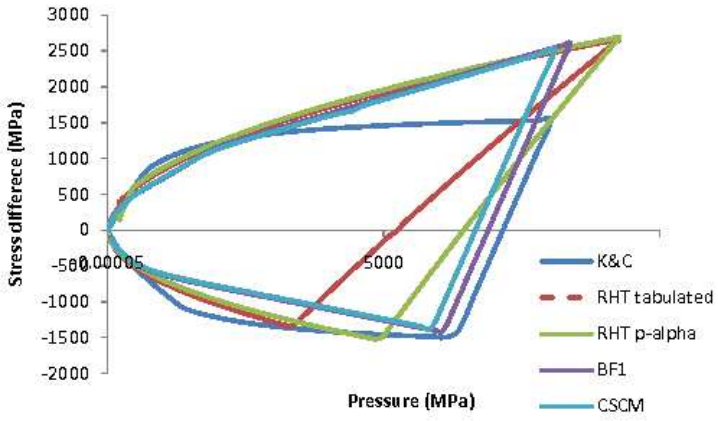


**Figure 6.5.** Comparison of stress difference versus pressure under uniaxial strain. (The BF1 and CSCM models results are different not because of model differences but because the BF1 model was driven with logarithmic strain, whereas the CSCM model was run using engineering strain.)

**Table 6.5.** Input parameters for the steel projectile

| Property | value |
|---|---|
| Density (kg/m$^3$) | 7800 |
| Modulus of elasticity (GPa) | 207 |
| Initial velocity (m/s) | 617 |
| Shear modulus (GPa) | 81.8 |
| Yield stress (MPa), $A$ | 1539 |
| Hardening constant (MPa), $B$ | 477 |
| Hardening exponent, $n$ | 0.18 |
| Strain rate constant, $C$ | 0.012 |

**Table 6.6.** Input parameters for the RHT concrete target

| Property | value |
|---|---|
| Density (kg/m$^3$), $\rho$ | 2770 |
| Shear modulus (GPa), $G$ | 25 |
| Compressive strength (MPa) | 153 |
| Tensile strength, $f_t/f_c$ | 0.054 |
| Shear strength, $f_s/f_c$ | 0.3 |
| Limit surface parameter, $A$ | 2.2 |
| Limit surface parameter, $N$ | 0.5 |
| Tensile/compressive meridian ratio, $Q_o$ | 0.6805 |
| Brittle to ductile transition, $BQ$ | 0.0105 |
| $G_{\text{elastic}}/G_{\text{elastic - plastic}}$, $PREFACT$ | 2.0 |
| Elastic strength/$f_t$, $TENSRAT$ | 0.8 |
| Elastic strength/$f_c$, $COMPRAT$ | 0.75 |
| Cap on yield surface | enable |
| Residual surface parameter, $B$ | 1.8 |
| Residual surface parameter, $M$, | 0.55 |
| Compressive strain rate exponent, $\alpha$ | 0.01 |
| Tension strain rate exponent, $\delta$, | 0.013 |
| Maximum fracture strength ratio | $1 \times 10^{20}$ |
| Damage constant, $D_1$ | 0.04 |
| Damage constant, $D_2$ | 1.0 |
| Minimum strain to failure | 0.01 |
| Residual shear modulus ratio, $SHRATD$ | 0.13 |
| Principal tensile failure stress (Pa) | $8.2 \times 10^6$ |
| Maximum principal stress difference/2 | $1 \times 10^{20}$ |
| Fracture energy (J/m$^2$) | 162 |
| Flow rule | radial return |
| Stochastic failure | none |

**Table 6.7.** Input parameters for the CSCM concrete target

| Property | value |
|---|---|
| Density (kg/m$^3$), $\rho$ | 2770 |
| Maximum strain increment | default |
| Rate effect | disable |
| Elements erosion criterion | 1.5 |
| Modulus recovery in compression, | enable |
| Cap retraction | none |
| Preexisting damage | none |
| Shear modulus (GPa), $G$ | 25 |
| Bulk modulus (GPa), $K$ | 28.43 |
| TXC surface parameter (Pa), $\alpha$ | $4.19 \times 10^8$ |
| TXC surface parameter (1/Pa), $\beta$ | $1 \times 10^{-9}$ |
| TXC surface parameter (Pa), $\lambda$ | $3.89 \times 10^8$ |
| TXC surface parameter, $\theta$ | 0.0433 |
| TOR surface parameter, $\alpha_1$ | 0.761 |
| TOR surface parameter (1/Pa), $\beta_1$ | 0 |
| TOR surface parameter, $\lambda_1$ | 0 |
| TOR surface parameter (1/Pa), $\theta_1$ | $2 \times 10^{-5}$ |
| TXE surface parameter, $\alpha_2$ | 0.68 |
| TXE surface parameter (1/Pa), $\beta_2$ | 0 |
| TXE surface parameter, $\lambda_2$ | 0 |
| TXE surface parameter (1/Pa), $\theta_2$ | $2.29 \times 10^{-5}$ |
| Hardening initiation $N_H$ and rate $C_H$ | 0.0 and 0.0 |
| Cap aspect ratio $R$ and initial location $X_o$ (Pa) | 5.0, $6 \times 10^8$ |
| Maximum plastic volume compaction, $W$ | 0.7434 |
| Linear shape parameter (1/Pa), $D_1$ | $6 \times 10^{-10}$ |
| Quadratic shape parameter (1/Pa$^2$), $D_2$ | 0 |
| Ductile and brittle softening parameter, $B$ and $D$ | 100 and 0.1 |
| Fracture energy in uniaxial compression (N/m), $G_{fc}$ | 16200 |
| Fracture energy in uniaxial tension (N/m), $G_{ft}$ | 162 |
| Fracture energy in pure shear (N/m), $G_{fs}$ | 162 |
| Shear-to-compression transition parameter, *pwrc* | 5.0 |
| Shear-to-tension transition parameter, *pwrt* | 1.0 |
| Modify moderate pressure softening parameter, *pmod* | 1.0 |
| Compressive rate effect and exponent, $\eta_{0c}$ and $N_{0c}$ | $1.83 \times 10^{-4}$ and 0.504 |
| Tensile rate effect and exponent, $\eta_{0t}$ and $N_{0t}$ | $1.76 \times 10^{-5}$ and 0.560 |
| Maximum overstress allowed in compression (Pa), *overc* | $1.05 \times 10^8$ |
| Maximum overstress allowed in tension (Pa), *overt* | $7.76 \times 10^6$ |
| Ratio of fluidity parameters, *srate* | 1.0 |
| Fracture energy rate effect parameter | 1.0 |

The contour plots of damage prediction by the RHT and CSCM models are illustrated in Figs. 6.6 and 6.7. Despite claims that inclusion of scale effects eliminates mesh dependence, it is clear from the pattern of radial cracking and from the shape of the perforation that the mesh texture strongly influences how the damage is distributed. As explained in [5], deterministic damage models of the type surveyed in this report are incapable of predicting realistic radial cracking even if they include scale effects for damage. This fact is why the BF1 model does *not* include scale effects. Instead, the BFS extension of the BF1 model incorporates scale effects as a natural consequence of statistical heterogeneity of the material strength, thus leading to a statistically mesh independent prediction for the number and orientation of radial cracks. Specifically, the BFS extension generates random realizations of the BF1 parameters based on scaling the size of the finite element relative to the specimen size used in the BF1 model parameterization.

As mentioned earlier, our perforation case study aims to reproduce the analysis in [37], which used the K&C model in an older version of LS-DYNA. Similar number of nodes and elements are used in our simulations. However, in the current version of LS-DYNA, this problem fails to run to completion even though it uses identical parameters, geometry, and boundary conditions. When fitting the data of $DIF$ given in [37] to both models, perforations in the concrete targets are not predicted. The penetrations in both RHT and CSCM simulations stop at approximately 2/3 of the target's thickness.

When the $DIF$ values are close to unity, the simulations using the RHT and CSCM models predict perforation. The size of the impact crater predicted by the RHT model is much smaller than that in [37] for the K&C model. The CSCM, on the other hand, shows the crater of a comparable size. The RHT, CSCM and the previously published K&C simulation [37] exhibit double cracks in the coordinate direction, and single cracks at 45°. Such spurious behavior is typical of deterministic smeared damage models. As the mesh is refined, it is expected that the number of radial cracks will increase, thus indicating non-predictiveness of smeared damage models even when they include scale effects for fracture energy. The severe mesh dependence of smeared damage models is also noted in a systematic study by Timmel, et al. [36].

As shown in Table 6.8, none of the smeared damage models are able to predict the residual velocity of 291 m/s that was observed in the experiment.

**Table 6.8.** Residual velocity comparison

| Material models | impact velocity (m/s) | residual velocity (m/s) |
|---|---|---|
| Experiment [37] | 617 | 291 |
| K&C [37] | 617 | 320 |
| RHT | 617 | 264 |
| CSCM | 617 | 327 |

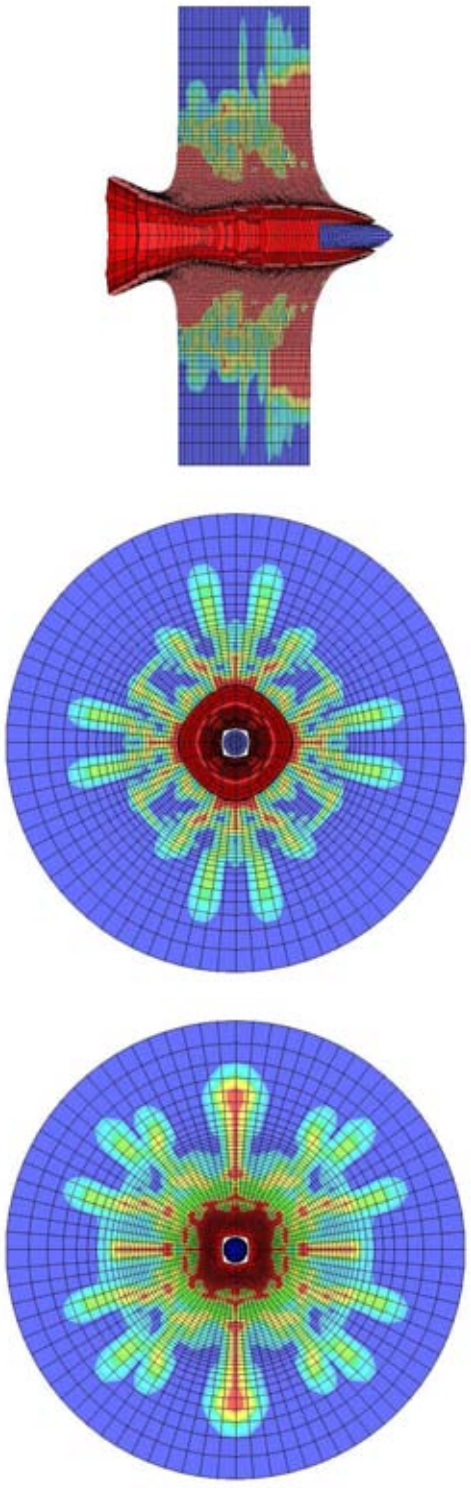

**Figure 6.6.** RHT Model: Contour plots of damage: side, front, and back view of the target (top to bottom).

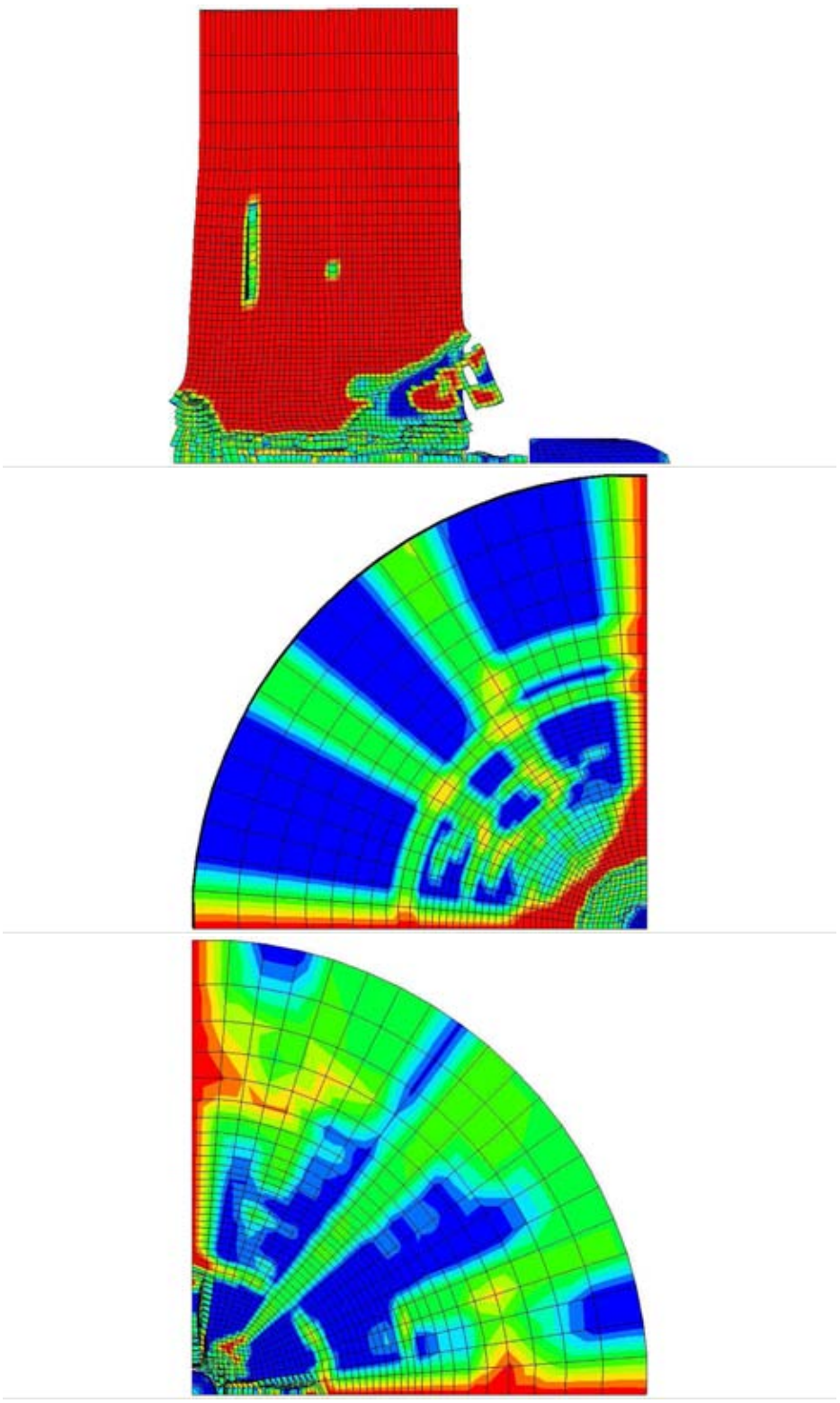

**Figure 6.7.** CSCM Model: Contour plots of damage: side, front, and back view of the target (top to bottom).

# Verification

Verification is evidence that the equations are solved correctly. We could find no evidence of systematic verification protocols for either the K&C, RHT, or CSCM models. Some potential for verification issues have been identified, but not aggressively investigated by these developers. For example, existence of a vertex in the failure surface of the K&C models was noted [28], but dismissed with the comment that "this does not violate any fundamental theoretical requirement. In fact, due to the use of a Prandtl-Reuss flow rule as implemented with the radial return algorithm, it creates no numerical difficulties either." Very little is said in the K&C, RHT, and CSCM publications about mesh dependence other than an unsubstantiated claim that inclusion of a length scale in fracture energy eliminates mesh dependency.

In contrast to the K&C, RHT, and CSCM models, the BF1 model uses the following verification practices:

- Demonstration of mesh dependency that led to an enhanced form of the BF1 model (called BFS) that accounts for scale dependent statistical uncertainty of strength, thus mitigating (not eliminating) mesh dependency while also reproducing the massive uncertainty in experimental data for concrete.
- Identification of three possible types of vertices in the failure surface and implementation of vertex handling that has been verified against analytical solution.
- Run time monitoring of solution quality with remote debugging. Without access to the K&C, RHT, and CSCM source codes, it is uncertain how these models deal with inadmissible results such as an erroneous prediction of a negative consistency parameter. If the BF1 model encounters such a problem, it terminates the calculation by issuing a debugging file that can be sent to the model developer for a bug fix followed by a rapid re-release of a corrected model (often within 48 hours).
- Automated scripts that allow assembly of version-controlled releases of the model in forms: an F77 version, an F90 version, and two stand-alone model driver versions. Automation of the release ensures identical source code on multiple platforms.
- Driver regression and benchmark testing involving approximately 30 test problems using three material data sets (thus totaling 90 tests) that must either pass before a new version is released or, if they do not pass, a "known bug" comment must be included in the release documentation.
- Genuine verification testing against analytical solutions. Unlike the K&C and RHT models, BF1 is capable of reducing to simpler idealized models for which agreement with analytical solutions has been confirmed.
- Pseudo verification testing for expected trends in solution as parameters are changed.
- Robustness verification achieved through benchmarks that target common problem areas such as loading past a vertex, loading that is highly tangential to the failure surface, running

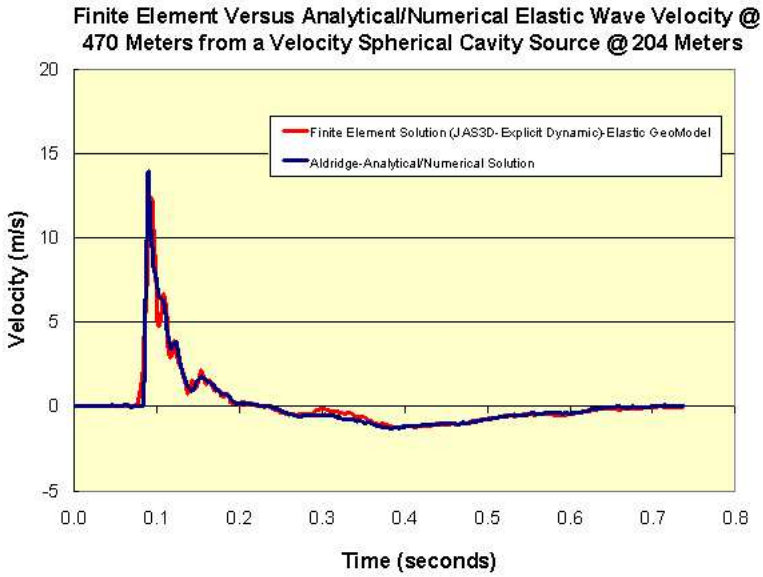


**Figure 6.8.** FEA vs. analytical/numerical elastic wave velocity example

with an inordinately large time step to ensure proper subcycling, dramatic transients in the loading direction, massive strains, etc.

- Rate of convergence testing with and without subcycling demonstrating first order convergence. Note: second-order convergence has not been attempted since it would require not only strain rate $\dot{\varepsilon}$, but also strain acceleration $\ddot{\varepsilon}$.

- Limited field-scale verification testing to reveal issues not attributable to the constitutive model. In situations where analysts have suspected a verification or validation problem with the BF1 model, the BF1 developers have designed verification tests that ultimately showed the bug to reside in the host code, not the constitutive model. The good agreement of the BF1 model for the elastic problem in Fig. 6.8 for example, was not achieved until artificial viscosity was repaired in the host codes that were attempting the inelastic validation of that problem. The BF1's remote debugging capabilities have also led to discovery of errors in host code advection of tensor fields as well as more routine problems such as user input mistakes (most commonly confusion between uniaxial effective strength and effective shear strength).

- Extensive documentation. The BF1 model has two components: the base model for the nonsoftening case and damage theory for softening. A detailed user's guide for the nonsoftening component that documents the theory for relatively new users is available [12]. It also

outlines the numerical solver; summarizes verification and validation tests, provides step-by-step parameterization instructions, summarizes input parameter symbols and keywords (with cross-referencing to relevant theory equations); provides input sets for several materials (including high- and low-strength concrete), and shows how to set input for reducing the model to simpler idealizations (Hooke's law, von Mises plasticity, Mohr-Coulomb, etc) for verification testing. The more recent BFS changes to the BF1 model have not yet been documented.

- Run-time input "sanity" checking with automated defaults. The BF1 model has 40 possible inputs keywords, but the number of inputs that are actually required scales appropriately with the complexity of the problem. If, for example, the user wishes to run linear elasticity, then only two parameters (bulk and shear modulus) are needed. All user input is checked at run time for physical or mathematical admissibility (e.g. bulk modulus must be positive). Reasonable defaults are set for unspecified parameters (e.g. associativity is imposed unless the user explicitly requests non-associativity).

- Portability. The BF1 model conforms to the Model Interface Guidelines [4], which has allowed it to be implemented in five different host codes, all using identical source code. An installation of the model at LLNL took only one day of the BF1's developer's time. Moreover, this broad use of the model has exercised it on numerous computing platforms using multiple compilers, thereby correcting minor numerical issues such as convergence criteria, along the way.

The above list of software SQA practices is perhaps what distinguishes the BF1 model from other models more than any other metric. Rising up to these SQA standards might lead to apparent delays in the implementation of new model features but it is believed that they ultimately reduce the total time required to achieve trustworthy, physically meaningful, simulations.

It should be noted that similar to the BF1 model, the CSCM model provides extensive documentation that gives an overview of the theory, as well as examples of how to used the model in LS-DYNA. The K&C model has documentation that provide such information, but the detailed documentation is available only for the Release II of the model. The K&C Concrete Release III is the latest release, which has a user guide that focuses on helping users getting started. No theoretical details are given with this current release.

# Validation

As parts of commercial packages, the K&C and RHT models have been used and validated by many authors. This chapter presents and summarizes the findings from some of these works.

## K&C: drop weight tests

In drop weight tests performed at FOI (FOA), the K&C model's ability to predict the material and structural response was evaluated [17]. In the tests, four reinforced concrete beams were subjected to impact loading using a drop weight. Hansson *et al.* [17], showed that the simulation was able to replicate the cracks in mode I, similar to the test results, but also predicted a mode II crack from the center point of impact that was not observed in the experiment.

## K&C: simulations of penetration and perforation of high performance concrete

Simulations of penetration and perforation of three types of high performance concrete targets were performed to assess the K&C model's ability to predict depth of penetration or residual velocity. A 6.3kg armor piercing steel projectile with an ogive nose radius of 127mm, length of 225mm, and diameter of 75mm was fired at the targets at zero impact angle and 620m/s velocity. The targets had a diameter of 1400mm. The target's lengths of 400mm and 800mm were used for the perforation and penetration tests, respectively. Unosson [37] showed that the model yielded good agreement with test data for perforation, but unsatisfactory results for penetration. Different element size was not able to be used in one material definition, and the damage curve was fitted only to one specific element size. As a result, an incorrect fracture energy release was computed, resulting in excessive amounts of shear damage in the element transition zone. When *DIF* (see Section 2) was used in the model, its effect lasted only to half the targets depth, beyond which changes in *DIF* had no effect.

## K&C: explosive wall breaching

Double-reinforced concrete slabs having dimensions of $2.4\times2.4\times0.2$m were subjected to the explosive loading environments produced by contact detonation charges. Akers *et al.* [2], showed in their work that the K&C model predicted a hole in the slabs close to the experimental value. However, the damage in the slabs was found to be excessive. No detailed explanations regarding the incorrect damage prediction were given in [2]. However, the tendency of this class of model to over-predict damage is well known and believed by some researchers [5] to be attributable to determinism (i.e. lack of statistical variability) that prevents localized failure in the form of discrete crack networks. Incorporating both scale effects statistical variability in properties dramatically reduces the phenomenon of excessive damage.

## K&C: vehicle-barrier crash test simulations

Numerical simulations for triaxial loading were conducted on plain concrete and compared to the experimental data. The calibrated K&C parameters were used to simulate a vehicle impact/crash

into a concrete barrier. Under triaxial tests, the parameters were tuned until the model showed correct linear and nonlinear response of the concrete in comparison to the experimental data [39]. Based on these well tuned parameters, a vehicle-barrier crash test was simulated. Yonten *et al.* [39] presented the comparison of the simulations using various concrete models available within the LS-DYNA program; each displayed different prediction from one another. No experimental data were used in assessing the vehicle-barrier crash test simulation results.

## RHT: simulation of penetration of high performance concrete

Simulations of a steel projectile penetrating a concrete target were presented and compared to experimental results in [18]. Hansson *et al.* [18] showed the influence of impact geometry on the calculated penetration path. For instance, a very small yaw angle had a large effect on the penetration path and exit velocity of the projectile in the simulation. The input data were tuned to match the penetration experiments but there was no mention of whether or not the alteration of parameters corrupted agreement with the original data on which the original parameters were based. It was also shown that the failure surfaces are dependent on pressure, strain rate, and triaxial stress state, and hence could handle most cases that are of "importance" for projectile penetration into brittle material like concrete. In addition, Hansson *et al.* [18] pointed out the difficulty of assessing the parameters that describe damage evolution, residual strength, and the tensile behavior and that new testing methods to determine damage development in concrete and strength of damage or partly damaged concrete still need to be developed. Some progress on measurement of damaged strength has been made by Chen *et al.* [7]. The BF1 model acknowledges this lack of data by defaulting an unspecified residual yield surface to that of sand.

## RHT: concrete subjected to projectile and fragment impacts

Leppänen [26] showed a simulation using the RHT model where a single fragment was shot against a concrete wall with impact velocities of 1024 m/s, 1163 m/s and 1238 m/s. At 1024 and 1163 m/s impact velocity, the calculation did not show the spalling evident in the experimental data, but scabbing behavior was correctly described. On the other hand, at 1238 m/s impact velocity, both spalling and scabbing behavior were correctly predicted.

## RHT: jumbo jet impacting on thick concrete walls

The RHT model was used by Katayama *et al.* [24] to simulate impact of a Boeing 747 passenger jet into a concrete wall. This three dimensional simulation was assessed for its ability to predict observed perforation, non-perforation, and spalling of the concrete. The model was able to predict the qualitative response of the concrete wall, but quantitative accuracy was not discussed in detail.

These are a few examples of existing simulations performed using the K&C and RHT concrete models. Both models appear to be very promising despite some weaknesses and existing flaws.

With parameter tuning, they seem to be able to capture the qualitative response of the concrete under impact but fail to accurately capture the damage in detail. Both models rely heavily on the data extracted from "correct/meaningful" experiments, which are not often available.

According to works cited here, the K&C model appears to work well in predicting perforation but not penetration. The excessive damage from penetration is largely caused by the element size dependency according to [37]. However, several improvements have been made since the model (LS-DYNA material 72) was evaluated, and a scaling factor that adjusts the fracture energy release depending on the element size has been included in the newer version (material 72R3). The K&C model includes tables and functions that are sophisticated enough to allow very accurate fitting to standard materials characterization experiments. However, predictiveness in general loading is still lacking.

For the RHT model, many benchmarks were performed to provide information for the model's basic parameters. However, these data are still not sufficient for the model to accurately capture the response at various strain rates. Similar to the K&C model, penetration is influenced heavily by the empirical data. While none of the works using the K&C model mentioned above discussed the effect of spalling and scabbing, simulations performed using the RHT model showed that these effects can be predicted to some degree.

# Chapter 7

# Conclusions

Four conventional damage plasticity models for concrete, K&C, RHT, BF1, and CSCM are compared. All four models use very similar elastic and inelastic computational procedures. All of the models support nonlinear elasticity, but with different formulations. All four models employ three strength surfaces: (1) yield surface, (2) limit surface, and (3) residual surface. Differences are seen in mathematical expressions defining the profiles of these strength surfaces.

The four models being compared differ in their softening evolution equations, as well as in their equations used to degrade the elastic stiffness. For all four models, scale effects are modeled differently. The K&C model requires that a particular material parameter affecting the damage evolution rate must be set by the user according to the mesh size to preserve energy to failure. Similarly, the BF1 model presumes that all material parameters are set to values appropriate to the scale of the element, and automated assignment of scale-appropriate values is available only through an enhanced implementation of BF1 (called BFS) that regards scale effects to be coupled to statistical variability of material properties. The RHT model appears to similarly support optional uncertainty and automated settings for scale dependent material parameters.

K&C and RHT support rate dependence by allowing the strength to be a function of strain rate, whereas the BF1 and CSCM models use Duvaut-Lion viscoplasticity theory to give a smoother prediction of transient effects. During softening, all four models require a certain amount of strain to develop before allowing significant damage accumulation. For K&C, RHT, and CSCM, the strain-to-failure is tied to fracture energy release, whereas a similar effect is achieved indirectly in the BF1 model by a time-based criterion that is tied to crack propagation speed.

All models investigated in this report rely heavily on well tuned parameters to reproduce observed material response. The BFS enhancement to the BF1 model automates the assignment of parameters based on experimentally justified scaling effects. There appears to be no barrier to adopting the best features of any of these models into one another. Therefore, any of these models could be used as a starting point to rectify deficiencies of smeared damage models and to then further enhance the physics of damage.

# References


[1] *Shock Wave Science and Technology Reference Library*, chapter Elements of Phenomenological Plasticity: Geometrical Insight, Computational Algorithms, and Topics in Shock Physics. Springer Berlin, 2007.

[2] S. Akers, R. Weed, D. Rickman, and Danielson K. Numerical simulations of explosive wall breaching. In *Proceedings of the Users Group Conference, 2005*.

[3] N. Bicanic and C. J. Pearce. Computational aspects of a softening plasticity model for plain concrete. *Mechanics of Cohesive-Frictional Materials*, 1:75–94, 1998.

[4] R. M. Brannon and Wong M. K. *MIG version 0.0 Model Interface Guidelines: Rules to Accelerate Installation of Numerical Models Into Any Compliant Parent Code*. Sandia National Laboratories Report SAND96-2000, Albuquerque, 1996.

[5] R. M. Brannon and J. M. Wells. Validating theories for brittle damage. *Metallurgical and Materials Transactions A*, 2007.

[6] Century Dynamics Ltd., Horsham. *AUTODYN: Theory Manual*, 4.3 edition, 2000.

[7] W. Chen and H. Luo. Dynamic compressive responses of intact and damaged ceramics from a single split hopkinson pressure bar experiment. *Experimental Mechanics*, 44(3):295–299, 2004.

[8] W. F. Chen. *Plasticity in Reinforced Concrete*. McGraw Hill, New York, 1982.

[9] J. K. Dienes and Q. H. Zuo. Impact initiation of explosives and propellants via statistical crack mechanics. *Journal of Mechanics and Physics of Solids*, 54(10):2235–2240, 2006.

[10] G. Duvaut and Lions J. L. *Les inequations en mecanique et en physique*. Springer-Verlag, Dunod, Paris, 1976. English transl.

[11] Federal Highway Administration, USA. *User Manual for LS-DYNA Concrete Material*, May 2007.

[12] A. F. Fossum and R. M. Brannon. *The SANDIA GEOMODEL Theory and User's Guide*. Sandia National Laboratories Report SAND2004-3226, Albuquerque, unlimited release edition, August 2004.

[13] A. F. Fossum and R. M. Brannon. Unified compaction/dilation, strain-rate sensitive, constitutive model for rock mechanics structural analysis applications. *ARMA/NARMS*, pages 04–546, 2004.

[14] A. F. Fossum and Brannon R. M. On a viscoplastic model for rocks with mechanism-dependent characteristic times. *Acta Geotechnica*, 1(2):89–106, September 2006.

[15] G. Gudehus. Elastoplastische stoffgleichungen fr trockenen sand. *Ingenieur Arch*, 42:151–169, 1973.

[16] K. Gylltoft. *Fracture mechanics models for fatigue in concrete structures*. PhD thesis, Luleå University of Technology, 1983.

[17] H. Hansson and P. Skoglund. *Structural Protection for Stationary/Mobile Tactical Behaviour 2001*. Technical Report. FOI Swedish Defence Research Agency: Weapon and Protection, Swedish Defence HQ, 2001.

[18] H. Hansson and P. Skoglund. *Simulation of Concrete penetration in 2D and 3D with the RHT Material Model*. Technical Report. FOI Swedish Defence Research Agency: Weapon and Protection, Swedish Defence HQ, 2002.

[19] A. Hillerborg. Analysis of fracture by means of the fictitious crack model, particularly for fibre reinforced concrete. *The Int. J. Cement Composites*, 2(4):177–184, 1980.

[20] A. Hillerborg. The theoretical basis of a method to determine the fracture energy $g_f$ of concrete. *Rilem Technical Commttees*, 18(106):291–296, 1985.

[21] G. R. Johnson and T. J. Holmquist. An improved computational constitutive model for brittle materials. In *High-pressure science and technology, Myrtle Beach, SC, 1993*.

[22] G. R. Johnson and T. J. Holmquist. Response of boron carbide subjected to large strains, high strain rates, and high pressures. *J. Applied Phys.*, 85:8060–8073, 1999.

[23] M. Kachanov. Anisotropic materials with interacting arbitrarily oriented cracks. In *Proceeding of the 14th U.S. Army Symposium on Solid Mechanics, Myrtle Beach, SC, 1996*.

[24] M. Katayama, M. Itoh, and R. Rainsberger. Numerical simulation of jumbo jet impacting on thick concrete walls - effects of reinforcement and wall thickness. In *The Second Asian Conference of High Pressure Research, Nara, Japan, 2004*.

[25] H. Kupfer, H. Hilsdorf, and H. Rush. Behavior of concrete under biaxial stresses. *ACI J.*, 66:656–666, 1969.

[26] J. Leppänen. Concrete subjected to projectile and fragment impacts: Modelling of crack softening and strain rate dependency in tension. *Int. J. Impact Engng*, 19(9-10):847–873, 1997.

[27] Livermore Software Technology Corporation, USA. *LS-DYNA: Keyword User's Manual*, May 2007.

[28] L. J. Malvar, J. E. Crawford, J. W. Wesevich, and D. Simons. A plasticity concrete material model for dyna 3d. *Int. J. Impact Engng*, 19(9-10):847–873, 1997.

[29] H. W. Meyers, Jr., and R. M. Brannon. *A Model for Statistical Variation of Fracture Properties in a Continuum Mechanics Code*. Army Research Laboratory, U.S.A., 2007.

[30] Y. D. Murray and B. A. Lewis. Numerical simulation of damage in concrete. Technical report, The Defense Nuclear Agency by APTEK, 1995.

[31] W. Riedel. *Beton unter dynamischen lasten, Meso- und makromechanische modelle und ihre parameter*. PhD thesis, EMI-Bericht 6/00, 2000.

[32] L. E. Schwer and Y. D. Murray. A three invariant smooth cap model with mixed hardening. *International Journal for Numerical and Analytical Methods in Geomechanics*, 18:657–688, 1994.

[33] P. E. Senseny, A. F. Fossum, and T. W. Pfeifle. Non-associative constitutive laws for low porosity rocks. *Int J Num Anal Meth Geomech*, 7:101–115, 1983.

[34] J. C. Simo and J. W. Ju. Strain and stress based continuum damage model. *Int J of Solids and Structures*, 23(7), 1987.

[35] Thomas Telford. *CEB-FIB Model Code 1990*. Lausanne, Switzerland, design code edition, 1993.

[36] M. Timmel, S. Kolling, P. Osterrieder, and P. A. Du Bois. A finite element model for impact simulation with laminated glass. *International Journal of Impact Engineering*, 34:1465–1478, 2007.

[37] M. Unosson. *Numerical simulation of penetration and perforation of high performance concrete with 75mm steel projectile*. User Report. Defence Research Establishment: Weapons and Protection Division, Tumba, Sweden, 2000.

[38] K. J. Willam and E. P. Warnke. Constitutive model for the triaxial behavior of concrete. In *ISMES Seminar on Concrete Structures Subjected to Triaxial Stresses, Bergamo, Italy, 1975*.

[39] K. Yonten, M. Manzari, A. Eskandarian, and D. Marzougui. An evaluation of constitutive models of concrete in ls-dyna finite element code. In *15th ASCE Engineering Mechanics Conference, New York, NY, 2002*.

# DISTRIBUTION:

Mechanical Engineering Department
University of Utah
50 S. Central Campus Drive, 2134 MEB
Salt Lake City, UT 84112

Professor Rebecca M. Brannon, Rebecca.Brannon@utah.edu
Seubpong Leelavanichkul, sleelava@eng.utah.edu

Lawrence Livermore National Laboratory
P.O. Box 808, M/S L-206
Livermore, CA 94551

Tarabay Antoun, Ph.D., antoun1@llnl.gov

Lawrence Livermore National Laboratory
P.O. Box 808, L-231
Livermore, CA 94551-9900

Joseph P. Morris, Ph.D., morris50@llnl.gov

Los Alamos National Laboratory
W-13, MS A142
Los Alamos, NM 87545

Matt Lewis, Ph.D., mlewis@lanl.gov

Center for Advanced Metallic and Ceramic Systems
Latrobe 122
Johns Hopkins University
3400 North Charles St.
Baltimore, MD 21218

Professor K. T. Ramesh, ramesh@jhu.edu

Northwestern University
2145 Sheridan Road, CEE Rm A135
Evanston, Illinois 60208-3109

Professor Zdenek P. Bazant, z-bazant@northwestern.edu

University of Colorado
Department of Civil, Environmental, and Architectural Engineering
1111 Engineering Dr.
428 UCB, ECOT 441
Boulder, CO 80309-0428

Professor Richard Regueiro, Richard.Regueiro@Colorado.edu

**Sandia Internal:**

Sandia National Laboratories
P. O. Box 5800
Albuquerque, NM 87185

Computational Shock & Multiphysics
MS 0378
R. M. Summers, rmsumme@sandia.gov
O. E. Strack, oestrac@sandia.gov

Computational Solid Mechanics & Structural Dynamics
MS 0380
J. Jung, jjung@sandia.gov
M. W. Heinstein, mwheins@sandia.gov
B. W. Spencer, bwspenc@sandia.gov

Geomechanics
MS 0751
S. J. Bauer, sjbauer@sandia.gov
T. Dewers, tdewers@sandia.gov
S. R. Sobolik, srsobol@sandia.gov

Solid Mechanics
MS 0372
J. V. Cox, jvcox@sandia.gov
H. E. Fang, hefang@sandia.gov
K. W. Gwinn, kwgwinn@sandia.gov
K. E. Metzinger, kemetzi@sandia.gov
J. T. Ostien, jtostie@sandia.gov
W. M. Scherzinger, wmscher@sandia.gov

Strategic Initiatives
MS 0372
J. Guadalupe Arguello, jgargue@sandia.gov
J. E. Bean, jebean@sandia.gov
J. E. Bishop, jebisho@sandia.gov

A. S. Gullerud, asgulle@sandia.gov
J. F. Holland, jfholla@sandia.gov
J. S. Rath, jsrath@sandia.gov
J. M. Redmond, jmredmo@sandia.gov
C. M. Stone, cmstone@sandia.gov

Mechanical Environments
MS 0847
S. W. Attaway, swattaw@sandia.gov

Mechanics of Materials
MS 9042
M. L. Chiesa, chiesa@sandia.gov

National Security Applications
MS 0751
L. S. Costin, lscosti@sandia.gov

Penetration Systems
MS 1160
D. A. Dederman, dadeder@sandia.gov
V. K. Luk, vkluk@sandia.gov

Performance Assessment & Decision Analysis
MS 1395
M. Y. Lee, mylee@sandia.gov

Structural Integrity & Licensing
MS 0744
M. F. Hessheimer, mfhessh@sandia.gov

Surety & GTS
MS 9042
E. P. Chen, epchen@sandia.gov

Technical Library, 9536 (electronic copy)
MS 0899

Sandia National Laboratories